AUTHOR(S): AHMED, R., DE VILLIERS LOVELOCK, H.L., FAISAL, N.H. and DAVIES, S.

TITLE: Structure-property relationships in a CoCrMo alloy at micro and nano-scales

YEAR: 2014

Publisher citation: AHMED, R., DE VILLIERS LOVELOCK, H.L., FAISAL, N.H. and DAVIES, S. 2014. Structure-property relationships in a CoCrMo alloy at micro and nano-scales. Tribology international [online], 80, pages 98-114. Available from: http://dx.doi.org/10.1016/j.triboint.2014.06.015

OpenAIR citation: AHMED, R., DE VILLIERS LOVELOCK, H.L., FAISAL, N.H. and DAVIES, S. 2014. Structure-property relationships in a CoCrMo alloy at micro and nano-scales. Tribology international, 80, pages 98-114. Held on OpenAIR [online]. Available from: http://openair.rgu.ac.uk

Structure-Property Relationships in a CoCrMo Alloy at Micro and Nano-scales

R. Ahmed[*] [a], **H. L. de Villiers Lovelock** [b, c], **N. H. Faisal** [d] and **S. Davies** [e]

[a] *Heriot-Watt University, School of Engineering and Physical Sciences, Edinburgh, EH14 4AS, UK*

[b] *TWI Ltd., Cambridge, CB21 6AL, UK (current);*[c] *Kennametal Stellite, Swindon, SN2 8UU, UK (previous)*

[d] *School of Engineering, Robert Gordon University, Schoolhill, Aberdeen, AB10 1FR, UK*

[e] *Bodycote HIP Ltd, Sheffield Road, Sheepbridge, Chesterfield, S41 9ED, UK*

Abstract

This investigation considered the multiscale tribo-mechanical evaluations of CoCrMo (Stellite®21) alloys manufactured via two different processing routes of casting and HIP-consolidation from powder (Hot Isostatic Pressing). These involved hardness, nanoscratch, impact toughness, abrasive wear and sliding wear evaluations using pin-on-disc and ball-on-flat tests. HIPing improved the nanoscratch and ball-on-flat sliding wear performance due to higher hardness and work-hardening rate of the metal matrix. The cast alloy however exhibited superior abrasive wear and self-mated pin-on-disc wear performance. The tribological properties were more strongly influenced by the CoCr matrix, which is demonstrated in nanoscratch analysis.

***Keywords*:** Nanotribology, nanoscratch, wear, manufacturing.

Research Highlights

1) Tribo-mechanical performance of Stellite 21 CoCrMo alloy manufactured via HIP-consolidation and by casting.
2) Nanoscale investigations highlighting the contribution of individual microstructural phases, and the influence of elasticity on non-dimensional penetration depth.

[*] Corresponding author, email: r.ahmed@hw.ac.uk, +44(0)1314513132

3) Nanoindentation, nanoscratch and modulus analysis of Stellite 21 alloys in order to elucidate the structure-property relationships.

1. Introduction

Although their hardness decreases as temperature increases, the cobalt based wear and corrosion resistant Stellite® alloys generally retain their wear resistance at high temperatures, where they also resist oxidation. They perform particularly well in lubrication starved or high temperature wear situations [1]. Originally developed by Elwood Haynes and patented in 1907 [2], many variations on the original CoCrWC and CoCrMoC alloys are now in common use. They generally contain 25-33 wt.% Cr, 4-18 wt.% W/Mo, and 0.1-3.3 wt.% C. Microstructurally, they consist of a CoCr(W,Mo) solid solution (with trace amounts of Ni, Fe, Si, Mn) containing one or more carbide phases. The solid solution matrix provides toughness whilst the carbides provide hardness and wear resistance as well as some strengthening. Cr is the principal carbide former, with W and Mo also playing a role. The relative amounts of W, Mo, Cr and the atomic ratio [W+Mo+Cr]:[C] strongly influence the types of carbides that form. Whilst the room temperature hardness is primarily a function of the carbide content, the hot hardness is more dependent on solid solution strengthening of the Co-based matrix by W and/or Mo [3].

Stellite 21 was developed in the mid-1930s. It consists of a CoCrMo alloy matrix containing dispersed hard carbides which strengthen the alloy and increase its hardness and wear resistance, but also decrease the ductility. The type, shape, size and distribution of the carbides is strongly influenced by the processing history of the alloy, and hence the mechanical properties and tribological performance are strongly dependent on the manufacturing route and any subsequent heat treatments. Due to the low carbide content relative to other similar alloys, the Co-based alloy matrix dominates the wear and corrosion properties, giving it excellent resistance to cavitation, galling, high-angle erosion and metal-to-metal sliding wear, but relatively low resistance to hard particle abrasion and low-angle erosion. The matrix can work harden considerably during wear or even during machining. Stellite 21 can be cast, powder metallurgically processed, or applied as a weld hardfacing. It is recommended for applications involving a combination of the above-mentioned wear mechanisms, combined with corrosion and/or high temperature service, such as valve trim for petrochemical and power generation. As a weld deposit it has been widely used in the building up of forging or hot stamping dies, due to its relatively good impact resistance [4].

The present authors have previously reported findings concerning the influence of a change in the manufacturing route from casting to HIPing in Stellite alloys containing between 4.6 and 16.5% W and between 0.7 and 2.4% C [5-8]. Compared with the cast alloys, the HIPed alloys had relatively finer, more rounded and homogeneously distributed carbides, which resulted in an

excellent combination of tribo-mechanical properties, i.e. an improvement in ductility, fracture toughness, and fatigue life, without compromising the hardness, strength and wear resistance. The emphasis in the current investigation is to consider if a similar improvement in performance of a low-carbon cobalt-based alloy containing Mo can be achieved by altering the manufacturing route from casting to HIPing.

Whilst the carbide content is the main differentiator between Stellite 21 and the alloys previously investigated (Stellite 4, Stellite 6 and Stellite 20), the fact that the alloy contains Mo instead of W can also influence the properties [5-8]. Firstly, it has been reported that replacement of W in Stellite 6K by Mo [9] or additions of Mo to Stellite 6 [10] result in changes in the carbide morphology and an increased volume fraction of carbides in the microstructure. This is ascribed to the fact that the atomic weight of Mo is roughly half of that of W, and hence the same mass percentage in an alloy translates to roughly twice as many Mo atoms as W atoms [9,10]. Mo also has a greater affinity for C than does W, thereby favouring the formation of carbides in the cast alloy [9]. Secondly, the corrosion behaviour of CoCrMo alloys is different to that of CoCrW alloys. For example, alloying with Mo rather than W improves the aqueous corrosion resistance in complex or reducing acidic environments [11].

Previous research on the tribological performance of Stellite 21 alloys has focused on the influence of alloying elements at room and elevated temperatures [12-15]. Huang et al. [12] investigated the influence of Mo content and heat treatment on the sliding wear resistance and concluded that both factors influenced the performance. Radu et al. [13] modified the composition of Stellite 21 alloy by adding yttrium and concluded that the addition of yttrium markedly enhanced the mechanical properties of the oxide scale on Stellite 21 and its adherence to the substrate, which benefited the high-temperature wear performance of the alloy in air. The benefit of oxide scale on the wear resistance of Stellite 21 was more pronounced in air than in an argon environment. However, the oxide scale became less protective as the wearing force was increased. The influence of manufacturing process has also been previously investigated in terms of cladding and surface coatings. Aoh et al. [14] investigated the wear behaviour of clad layers of Stellite 6 and 21 for hot rolling mill rollers and concluded that the elevated temperature sliding wear performance of Stellite 6 was superior to that of Stellite 21. Persson et al. [15] investigated the room temperature self-mated dry sliding performance of Stellite 21 and concluded that during high load dry sliding, a Co-enriched tribofilm is created which exhibits low friction and high galling

resistance. The tribofilm evolved via face-centred cubic (fcc) to hexagonally close-packed (hcp) phase transformation under strain.

Investigations relating to the tribological performance of Stellite 21 alloy manufactured via HIP-consolidation are however limited in the published literature. This paper provides microstructural and tribo-mechanical comparisons of cast and HIPed Stellite 21 alloys via Scanning Electron Microscopy (SEM), Energy Dispersive X-ray (EDX) spectrometry, X-Ray Diffractometry (XRD), hardness, abrasive wear, nanoscratch, and sliding wear evaluations.

2. Experimental Test Procedures

2.1. Materials and microstructure

Table 1 summarises the chemical compositions of the Stellite 21 alloys. The alloys were produced by casting and by HIP-consolidation of gas-atomised powders, respectively. The sieve analysis of the powder used for HIPing is summarised in Table 2. The powder was encapsulated in an air-free steel can and subjected to 100 MPa isostatic pressure at 1200˚C for 4 hours, followed by slow furnace cooling.

The microstructure of the powder and alloys was observed via SEM using a Secondary Electron (SE) imaging and also Back-scattered Electron (BSE) imaging detector. The chemical compositions of different phases developed in the powders and alloys were determined via both EDX and XRD with Cu-K_α radiation (wavelength = 1.5406Å). A commercially available open source software (ImageJ) was used to analyse the area fractions of each phase identified from the SEM images.

2.2. Hardness, modulus and impact toughness measurements

The Vickers macro- and micro-hardness of the alloys was measured using an Avery hardness tester under a load of 294N, and a Mitutoyo (MVK-H1) micro-hardness tester under a load of 2.94N, respectively. Five macro-hardness and ten micro-hardness measurements were conducted on each alloy. Spacing between measurements was maintained to ensure that neighbouring indents did not influence the hardness values as per BS-EN ISO 6507-1:1997 [16]. Nano-hardness and modulus measurements were performed using a calibrated nanoindentation system (NanoTest™ - Micro Materials Limited, UK) equipped with a standard Berkovich nanoindenter tip. Measurements were performed at room temperature (~23°C) in load control at loads of 50 mN and 5 mN to investigate the influence of nanoindentation load on measured hardness and modulus. The

indentation procedures were programmed as three segments of trapezoidal shape with 10 s loading, 5 s hold and 10 s unloading segments. Eighteen measurements were performed on each alloy at 50 mN load, and ten measurements at 5 mN load. Indentation hardness and modulus results were based on the real time load-displacement curve and were analysed using the Oliver and Pharr method [17]. Further details of the various measurement techniques and analysis in the nano-indentation method can be found in earlier publications [18-20].

Tensile tests were conducted according to BS-EN 10002 [21] on the HIPed specimens only, using an Instron® tensile testing machine (30 kN load cell, 5567 series). Dumbbell shaped test specimens of 25 mm gauge length and 4 mm diameter were used in this investigation. Three tests were conducted at a loading rate of 0.05 mm min^{-1}. The Charpy impact tests were conducted on unnotched alloy samples with dimensions of 10 mm × 10 mm × 55 mm, using an Avery Charpy impact tester at an impact rate of 5 m s^{-1}. Three tests were conducted on each alloy.

2.3. Nanoscratch sliding wear tests

The nanoscratch tests were conducted to investigate the micromechanics of plastic deformation and resulting wear of the individual metal matrix and carbide phases. Nanoscratch (sliding wear) tests were performed with a sphero-conical diamond indenter of 10 μm tip radius and 60° apex angle using the NanoTest™ system. This was akin to single asperity abrasive scratch wear of Stellite alloys with a view to understanding the role of individual microstructural features dominating the wear and deformation process. The scratch tests were performed as multi-pass tests at sliding velocity of 2 μm s^{-1} over a 60 μm track with (a) pre-scratch topographic scan, (b) a levelling distance followed by a ramped scratch, and (c) a post-scratch low load scan. In the pre-scratch and post-scratch scan the applied load was sufficiently low (10 μN) so that no wear occurred and was used to measure the topography of the scratch surface before and after the scratch test. Two different loading conditions were used during the scratch testing as summarized in Figure 1. In the 'on-load' scratch scan the load was ramped linearly after 20 μm travel at 5 mN/s to reach 100 mN for loading conditions 1. For the loading condition 2, the load was increased linearly after 20 μm travel at 50 mN s^{-1} to reach 100 mN. Six repeat tests were performed to test the reproducibility of the scratch behaviour for each of the loading conditions shown in Figure 1. The scratches were spaced 25 μm apart and it is expected that the probe is not deflecting the path when it encounters a large carbide phase in the soft matrix. In terms of energy, which is represented by the area under the loading profile, 2 μJ and 3.83 μJ were calculated for loading

conditions 1 and 2 respectively. Post-scratch test imaging using atomic force microscopy (AFM) and SEM was also used to investigate the residual surface features. Wear volume was calculated by exporting the 3D map of the surface topography from AFM software (NanoSurf™) into MATLAB®. A computer code was written to calculate the volume below and above the mean plane using a trapezoidal rule representing scratch volume and pile-up volume, respectively. The computer code applied the routine of calculating the wear volume automatically using the mean plane to each row of 3D surface data in MATLAB®.

2.4 Abrasive wear tests

Dry Sand Rubber Wheel (DSRW) abrasion tests (according to ASTM G65 Standard (Procedure B)) [22] were conducted to evaluate the abrasive wear performance. During each test, the alloy sample with dimensions of 6 mm × 25 mm × 75 mm, was forced under a load of 130 N against the rubber wheel, which rotated at a speed of 200±5 rpm. The outer polyurethane rim of the wheel had a diameter of 228.6 mm and a hardness of Shore A-60. Silica sand particles were used as the abrasive in this investigation. These sand particles were dry and rounded and had a size distribution of 85 wt.% particles in the range of 90-180 μm. The silica sand was introduced between the alloy sample and the rubber wheel, with a sand flow rate of 330 g min^{-1}. Each test lasted a total of 2000 revolutions, which was controlled by a revolution counter. Three tests were conducted on each alloy material. The wear mass loss of the sample was weighed to the nearest 0.001 g. The abrasive wear test results were reported as volume loss, which was computed from the mass loss and density of the alloy.

2.5 Sliding wear tests

The sliding wear resistance was evaluated via two different test methods, i.e. self-mated pin-on-disc tests, and ball-on-flat tests wearing against a WC-Co ball. Both tests were conducted at room temperature on a bench mounted wear test machine.

The self-mated pin-on-disc tests were conducted at a normal load of 25 N. The pin had a diameter of 6 mm and a length of 19 mm. The disc had a diameter of 31 mm and thickness of 8 mm. The surface roughness (R_q) of the discs was 0.1 μm. The test methodology was consistent with ASTM G133-02, Procedure A [23], except that the tip radius of the pin was 10 mm instead of 4.76 mm. During the test, the disc experienced reciprocating sliding motion at an oscillating frequency of 5 Hz and a stroke length of 10 mm. The total sliding distance was 100 m for each test. Three tests were conducted on each alloy. The wear surfaces of the pin and the disc were

measured via an interferometer (Zygo New View). The volume loss of the pin was computed from the scar diameter, and the volume loss of the disc was computed from the length of stroke and the average cross-sectional area of the wear grooves measured via an interferometer.

The ball-on-flat tests were conducted using a WC-Co ball (93.5-94.5 wt.% WC, and 5.5-6.5 wt.% Co) and an alloy disc sample under a normal load of 25 N. The ball radius was 6.35 mm. The disc had the same dimensions as those used in the pin-on-disc tests. During the test, the disc experienced reciprocating sliding motion at an oscillating frequency of 1 Hz, with a stroke length of 10 mm. The total sliding distance was 500 m for each test. Three tests were conducted on each alloy. The wear volume loss of the discs was computed from the length of the stroke and the average cross-sectional area of the wear grooves, which was measured via the interferometer.

3. Results

3.1. Chemical composition, microstructure and phase analysis

The HIPed version of the alloy (Table 1) contains significantly more Fe, Ni, Si and Mn than the cast alloy, as well as slightly less Mo. The composition of HIPed alloy is within the specified range for this alloy [24]. Previous investigations on Stellite hardfacing alloys have indicated that Mo can provide improved wear resistance [10].

Figure 2 shows the surface and cross-sectional (obtained by preparing a resin-embedded mounted section) morphology of the powder particles. Based on the sieve analysis presented in Table 2, the powder particle in Fig. 2a,b is one of a very few larger particles, shown here to reveal the surface morphology after gas atomising (Fig. 2b).

Figure 3 shows the microstructures of the cast and HIPed alloys. The intermetallic phases identified by XRD are believed to be indistinguishable from the CoCr matrix at the magnifications used, either by virtue of their high degree of crystallographic congruence with the matrix and/or their size; transmission electron microscopy would probably be required to resolve them. There are both Cr-rich and Mo-rich carbides visible in the HIPed alloy, but the cast alloy contains only one type of carbide. The etched light microscope images indicate the carbide morphology. Tiny pores are also visible in the microstructure of both alloys.

The image analysis results of the area fractions of various phases for both cast and HIPed alloys are shown in Table 3, and the XRD diffractogram of the powder and the alloys are

presented in Figure 4. The powder consists primarily of a Co-based solid solution (labelled α-Co) with traces of Co_7Mo_6 intermetallic phases and $M_{23}C_6$ carbides (where M = (Cr,Mo), labelled $Cr_{23}C_6$). The HIPed alloy exhibits the same peaks as the starting powder, but with the addition of Mo-rich intermetallic phases (Co_3Mo/Co_2Mo_3) and Mo-rich carbides (see Section 4.1). The cast alloy has a simpler XRD diffractogram with only a Co-based solid solution (labelled α-Co) and traces of $M_{23}C_6$ carbides and Co_xMo_y intermetallic phases. There is an indication of traces of possible MoC in both alloy spectra. Note that the orientation of the lattice planes of the sampled surface affects the relative heights of the α-Co peaks, this depends on the orientation and size of the grains relative to the incoming X-rays.

3.2. Hardness, impact toughness and modulus

Table 4 summarises the average macro-, micro- and nano-hardness results of both alloys. The difference in measured average hardness due to the test load (indentation size effects) is indicated as the % difference between macro- and micro-hardness, and also at two test loads of 50 mN and 5 mN for the nanoindentation tests. Figure 5 shows the average elastic modulus values measured via the nano-indentation method. The lower and higher values of data based on the standard deviation in Figure 5 can be related to the elasticity of metal matrix and carbide phase, respectively. The carbide phase here is applied to both carbide types identified in Table 3. Figure 6 shows the optical image of the location of some nano-indentations on cast and HIPed alloys using the 5 mN test load. The macrohardness and nano-indentation hardness at 50 mN load of the HIPed alloy is higher, whereas the nanohardness difference at 5 mN load indicate an opposite trend which could be attributed to the indentation size effects (ISE) in terms of the ratio of the plastic/plastic work [8].

The unnotched Charpy impact test results are also shown in Table 4. SEM morphology of the fractured surfaces are shown in Figure 7. Both alloys showed high impact energy when compared to other Stellite alloys [7], with the cast Stellite 21 showing a relatively higher average value. This can be ascribed to the lower energy fracture path in the HIPed alloy, which appears to have followed prior powder particle and carbide boundaries (Fig. 7b,c), probably due to the higher hardness of the metal matrix phase and small carbide size of the HIPed alloy. The cast alloy exhibited a more plastic mode of failure (Fig. 7a).

The tensile test results for the HIPed Stellite 21 alloy are presented in Table 5, along with typical values for this alloy and the cast alloy [24]. The tensile strength and elongation are below

what would normally be expected for HIPed Stellite 21, and the lower elongation indicates a lower range of ductility for the HIPed alloy.

3.3 Nanoscratch sliding wear performance

AFM, SEM and topography imaging was conducted for all scratches considered in this investigation. Figure 8 shows typical scratch observation comparisons for loading condition 2. Figure 9 shows the AFM, scratch and post-scratch topography scratch scans along the length of the scratch, and SEM observations for loading condition 1. The scratch scan indicates the displacement of the indenter tip during scratch testing whereas the post-scratch scan indicates the topography of the scratch groove after the test. The difference between the scratch and post-scratch scans indicate the extent of elastic recovery after unloading. The displaced average wear volume and pile-up volume during scratch testing were evaluated using the MATLAB® code for all loading conditions is summarised in Figure 10.

3.4 Abrasive wear performance

Average abrasive wear volume loss after the DSRW tests is shown in Figure 11. The cast alloy had better abrasive wear resistance than its HIPed counterpart. Figure 12 presents the typical wear scars of both alloys after the tests. Abrasive grooves and carbide pull-out can be observed on both of the worn surfaces.

3.5 Pin-on-disc wear performance

The average volume loss results after the pin-on-disc tests are shown in Figure 13. Similar to the trend in abrasive wear performance, the cast alloy performed better than the HIPed counterpart. Figure 14 shows typical wear scars on the disc surfaces and wear debris for both cast and HIPed alloys. The wear surface morphology is fundamentally different for each alloy. The cast surface wear scar seems smoother with few large grooves, whereas the HIPed surface shows a multitude of smaller grooves running across the length of the wear scar surface. The differences in these wear scars also lead to different types of wear debris produced after the tests. The cast alloy debris has a powder-like morphology with typical size in submicron range, whereas the HIPed alloy produced debris varying in size from submicron to plate-like delamination debris.

3.6 Ball-on-flat wear performance

The wear volume loss results after ball-on-flat tests are presented in Fig. 15. In contrast to the abrasive and pin-on-disc wear performance, the HIPed alloy performed better than the cast counterpart. The SEM observations of the wear surfaces and resulting debris of both alloys are shown in Figure 16. The wear surface of the cast alloy was smoother when compared to its HIPed counterpart and also showed some surface delamination. Wear delamination debris was also observed in the case of cast alloy. Figure 17 shows the averaged friction coefficient values recoded during the ball-on-flat tests.

4. Discussion

4.1 Microstructure

The microstructure of cast Stellite 21 consists of CoCrMo solid solution with 5% area fraction of Mo-rich inter-dendritic carbides (Table 3), as shown in Fig. 3a,b. Three different types of carbide have previously been reported in Stellite 21 alloys [25-27], as detected by observing etched metallographic cross-sections. These are: 1) eutectic carbides with lamellar morphologies that form at grain boundaries; 2) discontinuous carbides with blocky or spherical appearance that form within the dendritic matrix; 3) intergranular carbides with blocky morphologies that form along the grain boundaries.

Apart from the Co matrix, the phases observed in this alloy (Fig. 4) appear to be a mixture of $M_{23}C_6$ carbides and Co-Mo intermetallic σ phases, as previously reported in the literature [28-30], where $M_{23}C_6$ is the predominant phase and is expected from the literature to have with a typical approximate composition of $(Cr_{0.77}Co_{0.15}Mo_{0.08})_{23}C_6$ [31]. Although the EDX spectrum indicates the possibility of MoC, this carbide has not previously been reported in Stellite 21 alloys. Figure 3c,d shows the fine microstructure of HIPed Stellite 21, which consists of a CoCrMo solid solution matrix with fine carbide particles. The dark phase, which accounted for 5.1% area fraction of the microstructure (Table 3), was identified via EDX analysis combined with XRD (Fig. 4) as $M_{23}C_6$ carbide, with the approximate composition of $(Cr_{0.71}Co_{0.20}Mo_{0.09})_{23}C_6$, which is similar to that previously reported in the literature [31]. The light phase (1.7% area fraction) was identified by EDX analysis as M_6C carbide, with approximate composition of $(Co_{0.49}Cr_{0.29}Mo_{0.22})_6C$, but this small amount of M_6C was not detected using XRD (Fig. 4c). Although the total area fraction of carbide in the HIPed Stellite 21 was higher than that in the cast alloy, probably due to the slightly higher carbon content in the HIPed alloy, both are relatively low in comparison to the other Stellite

alloys, as mentioned previously. Therefore the matrix plays a more dominant role in influencing the mechanical and wear properties of Stellite 21 alloy.

Given the abundance of carbide-formers present (Table 6), and bearing in mind that the M/C ratio is 3.83 in $M_{23}C_6$, it is unlikely that there would be any uncombined carbon remaining to be a constituent of solid solution matrix in either alloy. The relatively high percentage of Si in the HIPed alloy, combined with the residual Mo could potentially lead to the formation of brittle intermetallic Laves phases CoSiMo or Co_3SiMo, which could also compromise the toughness of the HIPed alloy. These phases were not detected by XRD, although they may still be present below the XRD detection limit.

The Co-based solid solution therefore contains the remaining Mo along with Cr and Co, and is strengthened by the larger atomic size of Mo (ion size: Mo = 1.36 Å; Cr = 1.25 Å; Co = 1.25 Å). As observed from the area fractions of carbides (Table 3), the lower proportion of Mo-rich carbides in the HIPed alloy indicated that there was relatively larger proportion of Mo in the HIPed alloy matrix. Higher proportion of Fe, Mn, Ni and Si (Table 1) in the HIPed alloy also contributed to differences in the composition of the metal matrix for the HIPed Stellite 21 alloy. Based on the CoCrMo-C phase diagram [32], the CoCrMo solid solution matrix is generally fcc at higher temperatures and hcp at room temperature. However, the fcc→hcp transformation for this alloy is very sluggish and as-cast Co-based alloys generally have an fcc structure at room temperature. The influence of this phase transformation, higher Mo, Ni, Fe, Mn and Si alloying contents in the metal matrix phase of HIPed alloy, carbide size and morphology on the tribo-mechanical properties is discussed in next sections.

4.2 Hardness and Modulus

Both the cast and HIPed Stellite 21 alloys had similar micro-hardness, whereas the macro-hardness of the HIPed alloy was 12.6% higher (Table 4). The HIPed Stellite 21 had slightly higher carbon content and carbide fraction, both of which would be beneficial to its hardness. The difference between the hardness values at macro- and micro-scales is attributed to indentation size effects [8] and also the difference in carbide size in comparison to the indentation size. The indentation diagonal was typically 4 mm for the macrohardness test and 400 μm for the microhardness tests. Both of these sizes were order(s) of magnitude bigger than the typical carbide size and hence these macro- and micro-scale indentations are not able to differentiate between the hardness contributions from carbide and metal matrix phases. The nanohardness tests however provided the

relative comparison. Nanohardness values measured at 50 mN load indicated a trend of higher average hardness for the HIPed alloy, which was consistent with the macrohardness measurements. More importantly, as indicated in Table 4, the matrix phase of the HIPed alloy showed significantly higher hardness (7.9 to 8.8 GPa) in comparison to the cast (5.9 to 6.9 GPa) counterpart. This is attributed to the higher Mo content retained in the metal matrix of the HIPed alloy as discussed earlier. Higher proportion of Fe, Ni, Si and Mn (Table 1) also contributed to this difference in the metal matrix hardness for the HIPed alloy. Nanohardness tests conducted at 50 mN load indicate that the carbide hardness was higher the cast alloy. This is partly attributed to the size of indentation which was typically 3 to 5 μm in dimension and hence smaller than the carbide of cast alloy but roughly the same size as that of carbides in the HIPed alloy. Nanohardness tests conducted at 5 mN load had a typical indentation size of 1 to 2 μm and a penetration depth of 150 nm. As a result the contribution of the elastic stress component increased for the given indentation load and hence the average hardness of both alloys also increased due to the relatively larger elastic recovery component of the elastic/plastic strain. These interpretations of nanohardness values however need to be considered as approximate instead of absolute differences because i) the carbide size in the HIPed alloy was smaller and rounded in nature instead of interdentritic, which will lead to lower values especially if the indenter lands on the edge of the carbide or the carbide is not well-supported by the underlying matrix, ii) the matrix hardness of both alloys can be influenced by the presence or absence of subsurface carbides which are not visible or the proximity to a neighbouring carbide.

The above findings of differences in the average hardness of both alloys is consistent with previous findings in literature. Cawley et al. [33] concluded that there was no significant difference in the bulk hardness of an as-cast and HIPed and heat treated CoCrMo alloy. However the effect of casting process variables on alloy hardness has been reported in several articles [34-35]. An as-cast CoCrMo alloy obtained using a metallic mould with water cooling was reported to have hardness 10% higher than the same alloy obtained using a sand mould with air cooling, which was attributed to the refinement of the microstructure due to the fast cooling rate of the former [34]. Heat treatment, e.g. aging at 720°C for more than 10 hours, could also improve the hardness of cast CoCrMo alloy [35].

The average value of elastic modulus measured via nanoindentation at 5 mN load indicated that that the cast alloy modulus was approximately 25% higher than the HIPed counterpart. The average value of elastic modulus (270±75 GPa) for the HIPed alloy was similar to the value of

244.6±5.4 GPa measured via tensile test method (Table 5). It can be observed from Figure 6 that the modulus values related to the carbide phase of the cast alloy (313 to 338 GPa) were significantly higher than the maximum values (251 to 275 GPa) observed in the HIPed alloy, which resulted in a higher overall average of modulus for the cast alloy (Figure 5). This difference in modulus indicates improved bonding within the microstructural phases and at the metal matrix/carbide boundaries in the cast alloy. This indicates that the ratio of elastic/plastic deformation will be different between the two alloys, and the elastic deformation and recovery will be lower for the cast alloy during elastic/plastic loading. At the higher load of 50 mN, the difference in measured modulus values is marginal as the ratio of elastic/plastic work decreases.

4.3 Charpy Impact Energy

The cast Stellite 21 had higher average unnotched impact energy than the HIPed Stellite 21, albeit also higher standard deviation of the test results (Table 4). This is contrary to the findings of previous investigations in higher-carbon Stellite alloys which have reported almost an order of magnitude increase in the impact energy of HIPed alloys [5-8]. Figure 7a shows the cast Stellite 21 fracture surface. The surface is rough, indicating plasticity of the matrix, and exhibits a number of microcracks. The cracks have propagated along the dendrites, indicating inter-dendritic fracture. The HIPed Stellite 21 fracture surface (Fig. 7b,c) indicates that the prior powder particle boundaries and the grain boundary carbides were the main propagation route, which led to macro-cracks and a faceted morphology when compared to the cast counterpart. The spherical morphology of powder particle boundaries (Fig. 2) and sieve analysis of the Stellite 21 powders (Table 2) indicates a typical powder size of ≈20μm, which is consistent with the morphology observed in Figure 7c. The most likely reason for the similar fracture energies of the HIPed and cast Stellite 21 is the very low carbide content in comparison to previously reported alloys [5-8], which fundamentally changes the nature of the fracture path. The three dimensional interdentritic network of large carbides in cast Stellite 4, 6 and 20 provides a continuous low-energy fracture path which dramatically lowers the Charpy impact strength. The effect can be seen by comparing the values of 12.2, 9.8 and 1.4 J which were measured for cast Stellite 6, 4 and 20 respectively [5-8], whereas both the cast and HIPed Stellite 21 in this investigation have a fracture toughness roughly an order of magnitude higher than this (≈125 J for cast and ≈95 J for HIPed). It appears therefore that in the absence of a brittle carbide network, the difference between HIPed and cast microstructures is much less pronounced and hence the fracture toughness of the HIPed alloy, which seems to be dominated by prior powder particle boundaries (Figure 7), is of the same order of magnitude as the cast alloy. Both the values are of the same order of magnitude as the

previously reported HIPed Stellite 6 value of 109 J, and much higher than the previously reported HIPed Stellite 4 and 20 values of 21 J and 9 J. The hardness of the matrix phase in the HIPed alloy was higher which may have contributed to its relatively lower toughness compared to the cast counterpart. The generally fine microstructure of the cast CoCrMo alloy is dense and exhibits good ductility, both of which are beneficial to impact toughness [26,28,36]. The higher standard deviation observed for the cast material is attributed to its relatively less homogeneous microstructure and more convoluted crack path, compared with the HIPed material.

4.4 Nanoscratch tests

Nanoscratch and cyclic nanoindentation tests are one of the most widely used effective methods for measuring the critical loads that are related to adhesion properties of thin films and coatings [37-38]. In the current investigation, the nanoscratch test methodology enabled the evaluation of nanoscale differences in the wear behaviour of metal matrix and carbide phases. During scratch testing, material failure can occur by tensile stress behind the probe (through-depth cracking) and also due to compressive stress, as the hard carbide can separate from the metal matrix phase either by cracking and lifting (buckling) or by full separation (chipping). In the current investigation the deformation behaviour of the Stellite 21 alloy was predominantly plastic with no evidence of fracture of carbides.

4.4.1 Carbide response during nanoscratch testing

The carbides in the cast Stellite 21 alloy did not indicate appreciable wear, deformation or fracture. Hence the nanoscratch response was dominated by the properties of the metal matrix phase. This is highlighted in Figures 8(a,b), which compares the AFM topography and post-scratch wear depth profile for scratch 1. The post-scratch profile between approximately 22 µm and 45 µm sliding distance in Figure 8b shows a decrease in contact depth from approximately 350 nm to 50 nm, when the probe scratched over the carbide phase. The light microscope insert and the AFM image in Figure 8a shows the carbide boundary location and shallower depth of scratch groove. This behaviour was consistent whenever the probe scratched over the carbide in the cast alloy. For the case of HIPed Stellite 21 alloy as shown in Figure 8d, there are some minor variations in contact depth, which may be related to the carbide probe contact interaction, however the carbides in the HIPed alloy were too small to have as prominent an effect as was observed for the cast alloy. The SEM investigations indicated that despite the relatively smaller carbide size in the HIPed alloy, the carbides were not pulled out during the nanoscratch tests.

4.4.2 Metal matrix phase during nanoscratch testing

Contrary to the response of carbides, the metal matrix phase in the cast Stellite 21 alloy plastically deformed with lower nanoscratch resistance in comparison to the HIPed alloy as shown in Figure 10. There was also evidence of the formation of shear bands at the edge of scratch, as marked by the arrows in Figures 9a,b. Shear bands were not observed in the HIPed Stellite 21 alloy (Figure 9c). The formation of shear bands during nanoscratch testing in Stellite alloys, metallic glasses, amorphous alloys and forged Al6061 alloy, have previously been reported in published literature [39-42]. Stellite 21 due to high cobalt and low carbide content is known to strain harden considerably and undergo strain dependent phase transformation [1-4]. The presence of shear bands in the cast alloy indicates a higher work-hardening rate and a higher tendency of strain induced phase transformation.

Klarstrom et al. [43] has indicated that alloying elements such as iron, manganese, nickel, and carbon tend to stabilize the fcc structure and increase stacking fault energy (SFE), whereas elements such as chromium, molybdenum, tungsten, and silicon tend to stabilize the hcp structure and decrease SFE. The fcc to hcp transformation reaction is quite sluggish even for pure cobalt. However, in metastable compositions, it can be promoted by cold work via a mechanism involving the coalescence of stacking faults. The fcc structure has many slip systems for dislocations to cross slip onto, hence implying a low work hardening rate. However, the SFE of Co is relatively low, about only 15-50 mJ/m^2 (the SFE of Ni is 128 mJ/m^2), which allows the dislocations to easily dissociate into partial dislocations separated by an area of stacking fault. The mobility of dislocations is thus restricted, and cross slip hardly occurs. Therefore the low SFE hinders the cross slip movement of dislocations, resulting in rapid and highly localised work hardening,. Hence, the relatively higher Mo content in the solid solution of HIPed Stellite 21 alloy, as discussed earlier in section 4.1, leads to a decrease in the SFE, which can result in more work hardening. However in the case of the cast alloy, due to the relatively higher SFE caused by the lower content of Mo in the matrix, there may be less work hardening. Similarly, the presence of relatively higher Mo, Ni, Si, Fe and Mn content in the metal matrix of HIPed alloy (Table 1) will coarsen the slip lines making dislocation flow difficult. Although SFE was not measured in the current investigation, it is postulated that both of these factors, along with the relatively higher hardness metal matrix in the HIPed Stellite 21 alloy resulted in lower average volume loss (Figure 10) and lower average wear scar depths (Figure 8) of the HIPed alloy [44]. The coarse carbide structure in the cast alloy also providing inadequate support to parts of the metal matrix e.g. the

contact depth of the relatively softer metal matrix phase of the cast alloy (approximately 300 nm in Figure 8b) is higher than the HIPed counterpart (approximately 250 nm in Figure 8d). A more uniform distribution of carbide phases (Figure 3c,d) in the HIPed alloy therefore provided better support to its metal matrix phase during nanoscratch testing.

The fcc to hcp transformation in cobalt-based alloys is not a phenomenon limited to nanoscale deformations e.g. Persson et al. [15] investigated the room temperature self-mated highly loaded dry sliding performance of laser clad Stellite 21 and concluded that during high load dry sliding, a Co-enriched tribofilm is created which exhibits low friction and high galling resistance. The tribofilm evolved via fcc to hcp phase transformation under strain. The martensitic transformation of Co from fcc to hcp also strengthens the alloy when it happens. The hcp structure has only one slip plane, indicating that it has limited dislocation mobility and high work hardening rates. However, for high carbon Stellite alloys such as Stellite 20, the influence of work hardening in the matrix on the mechanical properties and wear resistance is usually overshadowed by the contribution of carbides.

4.4.3 Single asperity scratch tests and abrasive wear

A recent investigation by Woldman et al. [45] considered the abrasive wear of steel using single asperity wear experiments. This investigation indicated that the wear volume during single asperity wear was dependent on the tip radius, which was considered in the range of 50 µm to 200 µm. They concluded that the smaller tip radius produced more wear than the larger tip radius, because at constant load the relative groove volume increases with decreasing tip radius. For comparative analysis between the two Stellite alloys a single tip radius of 10 µm is used in the current investigation. The analysis of penetration depth presented in the investigation by Woldman et al. [45] originated from an earlier investigation by Hokkirigawa and Kato [46], which considered ploughing, cutting and wedge formation during abrasive wear process using in-situ SEM measurements. They introduced a non-dimensional parameter based on the degree of penetration (D_p) to classify the abrasive wear process, which was described as:

$$D_p = \frac{2d}{w} = R\sqrt{\frac{\pi H_v}{2N}} - \sqrt{\frac{\pi H_v}{2N}R^2 - 1} \quad (1)$$

where R is the indenter tip radius (mm), w is the width of the scratch groove (mm), d is the depth of the groove (mm), H_v is the Vickers hardness (kg/mm^2) and N is the normal load (kg) on

the indenter as shown schematically in Figure 18. Based on the slip line field theory they equated the contact pressure with the hardness of the specimen (equation 2) to evaluate the severity of abrasive wear.

$$\frac{\pi\,(w/2)^2}{2} = \frac{N}{H_v} \qquad (2)$$

In the current investigation and also in the earlier investigation by Woldman et al. [45], the scratch groove dimensions were analysed with an AFM and confocal microscope, respectively. Based on the post-scratch AFM measurements, it was possible to measure "*2d*" and "*w*" to calculate the experimental value of D_p, i.e. $D_{p,exp} = \frac{2d}{w}$. The right hand side of equation 1 can be used to calculate the theoretical value of $D_{p,theory}$ [45-46]. Based on this analysis, in the current investigation the values of $D_{p,exp}$ and $D_{p,theory}$ can be calculated as 0.12 and 0.21, respectively. This difference between the values of $D_{p,exp}$ and $D_{p,theory}$ is similar to what was also observed by Woldman et al. [45], where they indicated that for the smaller tip radius of 50 µm, the experimentally measured values of D_p were almost half of those calculated from the relationship indicated by Hokkirigawa and Kato [46]. In the current paper, it is hypothesised that this difference between $D_{p,exp}$ and $D_{p,theory}$ can be minimised by considering the elasticity of the asperity contact. As the values of $D_{p,exp}$ considered above and also by Woldman et al. [45] were based on the post-scratch investigations using AFM and confocal microscopy, they relied on the residual plasticity of contact with no consideration of contact elasticity. The current paper not only considers the post-scratch residual plasticity via AFM measurements, but also the elastic plastic deformation measurement during the scratch. This can be understood by considering the scratch and post-scratch profiles in Figures 8 (b,d). The post scratch profiles in these figures indicate residual plastic deformation after the scratch test, whereas the scratch test profile indicates the contact depth (*d*) during the scratch, with both the elastic and plastic components of deformation. If the above analysis of $D_{p,exp} = \frac{2d}{w}$ is repeated based on the *d* value obtained from the scratch profile instead of the post-scratch profile, the value of $D_{p,exp}$ can be evaluated as ≈ 0.2, which is very similar to the theoretical value ($D_{p,theory}$) of 0.21 based on the relationship by Hokkirigawa and Kato [46].

Another aspect of investigation by Hokkirigawa and Kato [46] considered the classification of the abrasive wear mechanism in three different categories of ploughing, wedging and cutting. For the discussion purpose in the current paper, ploughing is considered as the formation of wear

groove in the trailing edge of asperity contact and indicates plastic deformation of the material, as schematically indicated in Figure 18. Wedging is defined as the material pile-up in front of the asperity (or indenter tip), whereas the chip formation leading to removal of material is referred as cutting (Figure 18). Hokkirigawa and Kato [46] indicated that the severity of abrasive wear mechanism changes from ploughing to wedging and finally to cutting, depending on the degree of penetration (D_p) and friction coefficient during contact. The friction coefficient was also related to the shear strength at the contact interface. In the current investigation, only ploughing with limited wedging was observed (Figures 8 and 9). According to Hokkirigawa and Kato [46] a D_p value of $\approx$ 0.2, for a steel of similar H_v value as Stellite 21, the abrasive failure mode is expected to be a combination of ploughing and wedging. This is similar to what is observed in the current investigation (Figures 8 and 9). However at higher values of D_p e.g. 0.4, according to Hokkirigawa and Kato [46], cutting or chipping is expected to be the dominant abrasive failure mode. The experimental set-up in the current investigation is not expected to follow this change in the abrasive failure mode to chipping at higher values of D_p. This is because of the difference in the environmental conditions in the experimental set-up of the current investigation and that of Hokkirigawa and Kato [46]. Investigation by Hokkirigawa and Kato [46] considered both dry and lubricated experiments (lubricated experiments using vacuum grease) under vacuum in the SEM, and hence observed high values of friction coefficient (and hence high shear strength at the contact interface) in the range of 1.5 to 2.0 during wedging of lubricated and unlubricated contacts, respectively, before a transition to respective lower values of 1.0 to 1.5 due to chipping and cutting. In the current set-up where experiments were done in an air environment, shear strength at the contact interface and hence friction coefficient is not expected to reach such high values. Further investigations of friction coefficient in air vs. D_p values should be performed to map the abrasive failure modes in the presence of oxygen.

Another aspect reported by Hokkirigawa and Kato [46] was the influence of asperity angle (θ) on the transition of abrasive wear from wedging to cutting. They related this transition based on a non-dimensional value (f) of contact shear stress divided by bulk shear stress, and indicated that e.g. for f =0.3, this transition occurs at $\theta \geq 30^o$. The value of θ in the current investigation was calculated between 15^o to 17^o, which is much smaller than the expected value for the transition of wedging to cutting. This is also consistent with the results of a recent investigation by Khellouki et al. [47] where the influence of attack angle, which is similar to the asperity angle (θ) considered by Hokkirigawa and Kato [46], on the abrasive failure mode was reported. Although the load used in the investigation by Khellouki et al. [47] was higher (1 to 20 N) than the load used in the current

investigation (0.1 N), they reported that at small value of θ = 10°, ploughing was observed as the failure mode, whereas at higher values of θ = 30° the wear mechanism was predominantly ploughing with some evidence of cutting. At higher values of θ = 45° the abrasive wear mechanism was predominantly cutting.

4.5 Abrasive Wear

Within the limits of the tribological test conditions, the volume loss of the cast and HIPed Stellite 21 during the DSRW tests was 14.11±0.11 mm^3 and 18.69±0.05 mm^3, respectively (Fig. 11). The observations of the wear scars (Fig. 12) indicated that ploughing was the dominant wear mechanism for both alloys whereas carbide pull-out was observed only for the HIPed alloy. Most grooves on the wear scars of both alloys were due to ploughing by the abrasive sand particles. There were two major factors which contributed to the superior performance of cast Stellite 21 alloy, i.e. *i*) shape and size of carbides and *ii*) role of work-hardening, as discussed below.

Hardness rather than toughness is the deciding factor in the abrasive wear resistance of a material. The hard carbides in both alloys were fine (Fig. 3), and accounted for only a small fraction of the microstructure. However, the carbides in HIPed alloy were not only finer but also not interconnected when compared to the three dimensional network for the case of inter-dendritic carbides in the cast alloy. As a result, the carbides in the cast alloy provided more resistance to abrasive wear when compared with the HIPed counterpart. For the DSRW test conditions used in this investigation, authors have previously provided a contact mechanics based model, indicating the elastic loading on a typical sand particle based upon a Hertzian contact model [5,7,8]. As the sand particles were rounded, for an approximate calculation they can be modelled as spheres of 150μm diameter on the basis of the size range of sand particles. Although it is almost impossible to know the exact number of sand particles, and the load shared by each of them within the contact region at a given time in this dynamic model, a conservative approach can be adapted to assume that the loading on a given sand particle can be of the order of 1% (1.3N) of the total normal load (130N) during the DSRW test. This is not unlikely given the fact that for an absolute minimum (idealised) loading of each sand particle, the load should be uniformly distributed within a single layer of sand particles (as multiple layers will mean less particles directly in contact with the alloy sample), within the apparent contact area (or wear scar area of typical dimensions 1.5 cm × 1 cm). This provides a maximum number of sand particles as ~6000 in a single layer for uniform loading, which can co-exist between the rubber wheel and alloy sample at any time. If each sand particle then carries equal load, (i.e. minimum loading condition), it will be of the order of 0.02N.

However, not all sand particles enter the contact region (less than 6000 particles) and are not loaded equally as load is maximum in the centre of rubber wheel-alloy sample interface, the assumption of 1% of total load can be justified as a first approximation. Based upon this model, the contact diameter ($2a$) calculated from Hertzian equation of elastic loading can be approximated as ≥20μm. This area will grow further with the increase in sand particle diameter, deviation from the sphericity of sand particles (Fig. 2), increase in loading of individual particles, plasticity effects, frictional effects, and roll/slide ratio.

Contact area of this dimension, based upon a conservative model, therefore indicates that the contact diameter was an order of magnitude bigger than the carbide size (approximately 1-3μm) in the HIPed alloy, which would make it easier for the carbides and matrix to be pulled-out simultaneously in the HIPed alloy. This is consistent with the carbide pull-out observed on the surface of HIPed alloy (Fig. 12b). Contrary to this, individual large blocky interconnected carbides in the cast alloy provided more resistance to abrasive wear.

The conservative model adapted above can be applied to calculate the D_p value (equation 1) of about 0.1 for a sand particle of 150 μm under a 1% load (1.3N). According to the model presented by Hokkirigawa and Kato [46], this value of D_p is expected to plough during abrasive wear process and unlikely to yield wedging or cutting. However, the SEM observations in Figure 12 not only indicate ploughing but also cutting and carbide pull-out. This difference is attributed to the fact that the sand particles are not ideally spherical and irregularities in sphericity of the sand particles will result in higher D_p values due to higher contact pressure. Moreover for the HIPed alloy, the carbides are much smaller in size than the sand particles, and hence carbide pull-out accelerates the DSRW abrasive wear due to higher D_p values. The value of asperity angle (θ) for the above sand abrasion model can be evaluated as 8°, which is much smaller than the expected value for the transition from wedging to cutting of about 30° [47]. As this contact deformation model of sand alloy interface is based on the Hertzian elastic contact, this value of 8° can be expected to double to ≈ 16° after incorporating the plastic component, which is still less than the reported value of 30° for the transition to chipping [47]. This doubling of θ value to ≈ 16° is based on the ratio of the elastic +plastic deformation to the plastic deformation, as observed in Figures 8(b,d) from the scratch and the post-scratch profiles, which indicates this ratio of ≈ 0.5.

An aspect not considered in the investigation by Hokkirigawa and Kato [46] and also Woldman et al. [45], was the role of fatigue cracking and work-hardening within the plastically

deformed ridges after repeated sliding of abrasive particles. This was investigated using multiple-pass scratch tests by Khellouki et al. [47]. They indicated that during multiple pass scratching the abrasive wear mechanisms can change from ploughing to cutting due to fatigue of instable wedges. Hence the cutting observed in the current DSRW tests in the current investigation is expected to be not only due to higher D_p values due to irregular surface of sand and the presence of carbides (due to carbide pull-out) in the contact region, but also due to the fatigue cracking and work-hardening of the plastically deforming ridges under repeated loading by the sand particles.

Despite slightly lower average macro-hardness and nanohardness of the metal matrix phase of the cast Stellite 21 alloy, it showed superior abrasive wear resistance than the HIPed counterpart, which can also be attributed to the higher work hardening rate of the cast alloy. As observed in the nanoscratch tests, the CoCr matrix of the cast Stellite 21 in this investigation can be expected to exhibit a higher work hardening rate than the HIPed alloy due to the differences in chemical composition. There was relatively higher intensity of ridges and grooves on the wear scar of cast alloy, as shown in Fig. 12a, which indicates that plastic deformation occurred extensively during the DSRW testing. The plastic deformation promoted work hardening of the Co-rich matrix, and subsequently enhanced the strength of the alloy, which provided extra abrasive wear resistance to the cast alloy. However for the HIPed alloy (Fig. 12b), the wear grooves are much shallower, smoother and narrower. It appears that plastic deformation in the HIPed alloy did not occur as extensively as in the cast alloy during the test, and hence work hardening will likewise have been less pronounced.

4.6 Pin-on-Disc Sliding Wear

The volume loss of cast Stellite 21 (Fig. 13) was much lower than that of the HIPed counterpart after the self-mated pin-on-disc tests. The observation on the wear scar of the cast alloy (Fig. 14a) showed that there were some pits and grooves on the worn surface. However the surface was generally smooth which is consistent with the small sized powdery debris indicating three body abrasion and micro-polishing of the surface. The pits were formed either due to carbide pull-out, or micro-cutting by abrasive particles or wear debris. The initial deformation on the surface could result in substantial work hardening on the cast Stellite 21 alloy, and hence the enhanced strength provided better wear resistance to both the pin and disc samples. Wear debris after the test, which consisted of 22.8 wt.% oxygen (based on the EDS analysis), indicating oxide layers could also have formed during the wear testing.

Figure 14c shows the wear scar of the HIPed Stellite 21. There were a number of smaller grooves formed due to ploughing during the test, indicating that the HIPed Stellite 21 could not resist ploughing due to three body abrasion of small sized carbides which were pulled out from the pin and disc surface. The ploughing grooves observed on the surface of HIPed alloy are larger than the typical carbide size, which made it easier for carbides to be pulled out, aggravating the three body abrasion wear process. As a result smaller and larger debris were produced for the HIPed Stellite 21 couple as shown in Fig. 14d. The granular morphology of most debris indicated that these debris increased wear volume of HIPed alloy in three-body abrasion. Hence as opposed to the nanoscratch test where carbides were not pulled out, higher load and carbide pull-out resulted in relatively poorer performance of the HIPed alloy.

4.7 Ball-on-Flat Sliding Wear

The volume loss of the cast and HIPed Stellite 21 alloys during the ball-on-flat tests was 0.43±0.10 mm^3 and 0.36±0.04 mm^3, respectively (Fig. 15). As the WC-Co ball was much harder than Stellite 21, ploughing dominated the material removal for the HIPed alloy, as indicated by the grooves on the worn surface. These grooves were deep and wide, with an estimated width of 40μm. There were also a few scratches, which was due to the fact that the carbide particles were dragged on the surface after being pulled out.

The grooves on the wear scar of the cast alloy (Fig. 16a) indicated that ploughing was also the main wear mechanism for the cast alloy. The plastic deformation due to the ploughing by the WC-Co ball could result in work hardening on the matrix, which would improve the strength and wear resistance. However, the volume loss of cast Stellite 21 was slightly higher than the HIPed Stellite 21 during the ball-on-disc tests, which is contrary to the fact that the cast alloy had a higher work hardening rate than the HIPed alloy. Closer investigation of the wear scar reveals that besides ploughing, delamination wear also occurred in the cast alloy , which is consistent with the sheet like delamination debris observed after the test (Fig. 16b).

According to the delamination theory of wear [48], when two sliding surfaces come into contact, asperities of the softer surface are easily deformed or fractured. Therefore the contact is more likely to be an asperity-plane contact. The softer surface experiences cyclic loading as the asperities of the harder surface plough it, which results in subsurface deformation. As the plastic shear deformation accumulates with repeated loading, cracks are nucleated below the surface. Further loading and deformation causes the cracks to propagate parallel to the surface, at a depth

which depends on the material properties and friction coefficient. When these cracks finally reach the surface at certain weak positions, flaky wear sheets 'delaminate'.

Different from the self-mated pin-on-disc test, the ball-on-flat test was carried out between Stellite alloy and a WC-Co ball, which is much harder in comparison with the alloy. The alloy surface therefore was ploughed easily, and the contact quickly changed to 'asperity-plane' contact. Moreover, the duration of the cyclic loading in the ball-on-flat test was much longer than that in the pin-on-disc testing. Therefore delamination wear occurred on the cast Stellite 21 alloy during the ball-on-flat tests. The wear scar at the bottom of groove in Fig. 16a was apparently due to the delamination wear, which resulted in much material removal. The plate-like debris shown in Fig. 16b were caused by both ploughing and delamination wear. The friction coefficient values shown in Figure 17 indicate very similar steady state averaged friction values and a similar standard deviation for both cast and HIPed alloys, indicating that there was no significant influence of this change in delamination failure mode on the frictional behaviour. This is not unusual as during steady state wear, the role of wear debris is expected to dominate friction and wear properties of both alloys.

The HIPed Stellite 21 did not experience the delamination wear during the ball-on-flat test, which could be attributed to two factors. Firstly, work hardening not only improves the strength of material, but also reduces the ductility. The HIPed Stellite 21 had a lower work hardening rate than the cast Stellite 21 due to the difference in chemical composition. During the wear testing, the strength of the HIPed alloy was lower, but its ductility was higher than the cast alloy. The relatively lower strength encouraged ploughing on the HIPed Stellite 21, which dominated the wear loss. However, the relatively higher ductility could efficiently hinder the initiation and propagation of cracks, and hence hindered the delamination wear. Secondly, the carbide/matrix boundaries in the relatively coarse microstructure of cast alloy were likely to be the main propagation routes for the subsurface cracks. However in the HIPed Stellite 21, the cracks were trapped in the matrix due to the finer microstructure of the HIPed alloy. It should be noted that the Charpy impact energy of the cast alloy was higher than the HIPed counterpart (Table 4). This difference is attributed to the nature of microscopic cracks in delamination wear, which propagate in the near surface shear stress due to asperity contact, as opposed to the macroscopic and tensile cracks in the Charpy impact tests. In conclusion, the cast alloy had a better resistance to ploughing than the HIPed alloy, but the delamination wear occurred during the tests due to the material

properties and experimental conditions, which resulted in slightly higher wear loss for the cast alloy.

5. Conclusions

A comparison of the structure property relationships in cast and HIPed Stellite 21 alloys was conducted. The findings indicate that the perceived benefits in tribo-mechanical properties for HIPed alloys (as compared to cast alloys) are less pronounced for lower carbon alloys, because the cast microstructure's behaviour is not dominated by a network of brittle hard carbides. Within the limits of the tribological conditions considered in this investigation, the conclusions can be summarised as follows:

1. HIPing of Stellite 21 alloy resulted in a finer carbide microstructure when compared to the cast counterpart, which had inter-dendritic Cr-rich and Mo-rich carbides.
2. Nanoscratch testing of HIPed and cast Stellite 21 alloys indicated differences in the wear behaviour at nanoscale between the metal matrix and carbide phases. The microstructural homogeneity and higher hardness of the metal matrix phase in the HIPed alloy led to relatively lower volume loss in comparison to the cast counterpart.
3. The difference between the experimentally measured values of non-dimensional penetration depth parameter ($D_{p,exp}$) and the theoretical parameter ($D_{p,theory}$) proposed by Hokkirigawa and Kato [46] can be minimised by considering the elasticity of the asperity contact.
4. The lower proportion of Mo rich carbides in the HIPed alloy indicated Mo was retained in the metal matrix phase, due to sluggish diffusion in the rapidly solidified gas atomised powder during HIPing, compared to the rapid diffusion that is possible in the melt during casting. This provided more resistance to plastic deformation in the matrix phase of the HIPed alloy due to roughening of slip planes and decrease in stacking fault energy. Shear bands were also observed in the cast alloy during nanoscratch testing indicating strain dependent transformation and a lower rate of work-hardening.
5. The finer microstructure and higher work hardening rate of the HIPed alloy (which is postulated due to lower SFE caused by higher Mo content [43]) however resulted in inferior DSRW and pin-on-disc wear performance as the properties are more dominated by the carbides.

6. The ball-on-flat tests however indicated higher wear resistance of the HIPed alloy which was attributed to the observations of contribution from delamination wear mechanism in the cast alloy.
7. Average hardness of both alloys was similar at microscale, however the HIPed alloy showed a 12.6% increase in average hardness at macro-scale and a 19.6% increase at nanoscale tests conducted at 50 mN load.
8. Cast Stellite 21 exhibited an average unnotched fracture toughness value nearly 8 times that of cast Stellite 6 [7] and nearly 10 times that of cast Stellite 4 [6], because it does not contain sufficient carbides to form a semi-continuous low-energy fracture path.
9. HIPed Stellite 21 exhibited an average unnotched fracture toughness value only marginally higher than that of HIPed Stellite 6 [7] but nearly 6 times that of HIPed Stellite 4 [6].
10. The difference between the unnotched fracture toughness of cast and HIPed Stellite 21 was much less pronounced than the difference between cast and HIPed versions of the higher carbon alloys that were previously investigated by these authors [5-8]. This is attributed to the absence of a network of brittle carbides in the cast alloy which meant that the crack propagation along prior powder particle boundaries in the HIPed alloy was marginally lower-energy than the fracture path in the cast alloy. This factor eliminated any benefits derived from the finer HIPed microstructure.

6 Acknowledgements: The authors acknowledge the financial support of Kennametal Stellite during for this work and the support of Dr Hao Yu while he was at Heriot-Watt University for his assistance in some of the experimental tests. Assistance from Mr Elameen in the scratch testing at Alfaisal University is also acknowledged.

References:

[1] K. C. Antony, Wear-resistant Cobalt-based Alloys, Journal of Metals, **5**(2) (1983) 52-60.

[2] E. Haynes, US Pat. No. 873,745; 1907.

[3] J.L. de Brouwer and D. Coutsouradis, Influence of tungsten and carbon contents on the microstructure and properties of a cobalt-base hardfacing alloy; Cobalt [32] September 1966, p. 141-147.

[4] P. Crook, Cobalt-base Alloys Resist Wear, Corrosion, and Heat, Advanced Alloys & Progress, **145**(4) (1994) 27-30.

[5] H. Yu, R. Ahmed, H.L. de Villiers Lovelock, A Comparison of the Tribo-mechanical Properties of wear-resistant cobalt based alloys produced by different manufacturing processes, Transactions of the ASME, **129** (2007) 586-594.

[6] H. Yu, R. Ahmed, H. de Villiers Lovelock and S. Davies, Tribo-Mechanical Evaluations of Cobalt-Based (Stellite 4) Alloys Manufactured via HIPing and Casting, Proceedings of the World Congress on Engineering 2007 Vol II, WCE 2007 London, U.K., July 2-4 (2007)

[7] H. Yu, R. Ahmed, H. de Villiers Lovelock and S. Davies, Influence of Manufacturing Process and Alloying Element Content on the Tribomechanical Properties of Cobalt-Based Alloys, ASME Journal of Tribology, **131**(1) (2009), p.011601-01 to 011601-12.

[8] R. Ahmed, H.L. de Villiers Lovelock, S. Davies, N. H. Faisal, Influence of re-HIPing on the structure property relationships of cobalt-based alloys, Tribology International, **57** (2012) 8-21.

[9] M.X. Yao, J.B.C. Wu, W. Xuc, R. Liu, Metallographic study and wear resistance of a high-C wrought Co-based alloy Stellite 706K, Materials Science and Engineering A, **407** (2005) 291–298.

[10] J-C. Shin, J-M Doh, J-K. Yoon, D-Y. Lee, J-S. Kim, Effect of molybdenum on the microstructure and wear resistance of cobalt-base Stellite hardfacing alloys, Surface and Coatings Technology **166** (2003) 117–126.

[11] M.X. Yao, J.B.C. Wu, Y. Xie, Wear, corrosion and cracking resistance of some W- or Mo-containing Stellite hardfacing alloys, Materials Science and Engineering: A, Volume 407, Issues 1–2, 25 October 2005, Pages 234-244, ISSN 0921-5093, http://dx.doi.org/10.1016/j.msea.2005.06.062.

[12] P. Huang, R. Liu, X. Wu, M. X. Yao, Effects of Molybdenum Content and Heat Treatment on Mechanical and Tribological Properties of a Low-Carbon Stellite Alloy, J. Eng. Mater. Technol. **129** (2007) 523-530.

[13] I. Radu, D.Y. Li, Investigation of the role of oxide scale on Stellite 21 modified with yttrium in resisting wear at elevated temperatures, Wear, **259(1–6)** (2005), 453–458.

[14] J. N. Aoha, Y. Jenga, E. Chua, L. Wub, On the wear behavior of surface clad layers under high temperature, Wear, 225–229(2), 1114–1122 (1999).

[15] D. H. Persson, E. Coronel, S. Jacobson, S. Jacobson, Surface analysis of laser cladded Stellite exposed to self-mated high load dry sliding, Wear, 261(1), 96–100 (2006).

[16] BS EN ISO 6507-1:1997 Metallic materials - Vickers hardness test - Part 1: Test method.

[17] W.C. Oliver, G.M. Pharr, An improved technique for determining hardness and elastic modulus using load and displacement sensing indentation experiments, Jr. Mater. Res. 7 (1992) 1564.

[18] R. Ahmed, N. H. Faisal, A. M. Paradowska, M. E. Fitzpatrick and K. A. Khor, Neutron diffraction residual strain measurements in nanostructured hydroxyapatite coatings for orthopaedic implants, Journal of Mechanical Behavior of Biomaterials, 4(8) (2011), 2043-2054.

[19] N.H. Faisal, R. Ahmed, R.L. Reuben, Indentation Testing and Its Acoustic Emission Response: Applications and Emerging Trends, Inter. Mater. Rev. 56 (2011) 98.

[20] R. Ahmed, Y. Q. Fu, N. H. Faisal, Fatigue at nanoscale: an integrated stiffness and depth sensing approach to investigate the mechanisms of failure in DLC film, ASME Jr. of Tribology, in print 2012.

[21] BS-EN10002- Tensile testing of metallic materials; Method of test at ambient temperature, USA.

[22] ASTM G65-00, Standard Test Method for Measuring Abrasion Using the Dry Sand/Rubber Wheel Apparatus, ASTM International, USA.

[23] ASTM, 2002, ASTM G133-02, *Standard Test Method for Linearly Reciprocating Ball-on-Flat Sliding Wear*, ASTM International, West Conshohocken, PA, USA.

[24] Deloro Stellite; Stellite 21 Technical Data Sheet, 2008, DS01-22208 (S R0808), http://www.stellite.co.uk/Portals/0/Completed%20Data%20Sheets/Stellite%2021%20DS01-22208%20(S%20R0808).pdf

[25] K. Asgar, F. A. Peyton, Effect of Microstructure on the Physical Properties of Cobalt-Base Alloys, Journal of Dental Research, 40(1), 63-72, (1961).

[26] M. Gomez, H. Mancha, A. Salinas, J. L. Rodriguez, J. Escobedo, M. Castro, M. Mendez, Relationship between Microstructure and Ductility of Investment Cast ASTM F-75 Implant Alloy, Journal of Biomedical Materials Research, 34, 157-163, (1997).

[27] F. S. Badge, W. O. Sweeney, Metallurgy of High Temperature Alloys Used on Current Gas Turbine Designs: Symposium on Material for Gas Turbine, ASTM, USA, 99, (1946).

[28] B. A. Boeck, T. H. Sanders, V. Anand, A. J. Hickl, P. Kumar, Relationships Between Processing, Microstructure, and Tensile Properties of Co-Cr-Mo Alloy, Powder Metallurgy, 28(2), 97-104, (1985).

[29] Caudillo, M. Herrera-Trejo, M. R. Castro, E. Ramirez, C. R. Gonzalez, J. I. Juarez, On Carbide Dissolution in an As-Cast ASTM F-75 Alloy, Journal of Biomedical Materials Research, 59(2), 378-385, (2002).

[30] A. J. T. Clemow, B. L. Daniell, Solution Treatment Behavior of Co-Cr-Mo Alloy, Journal of Biomedical Materials Research, 13(2), 265-279, (1979).

[31] W. V. Youdelis, O. Kwon, Carbide Phases in Cobalt Base Superalloy: Role of Nucleation Entropy in Refinement, Metal Science, 17(8), 379-384, (1983).

[32] S. R. Robertson, The effect of thermal and thermomechanical treatments on low carbon ASTM F75 alloys for possible use in prosthetic applications, Ph. D. Thesis, University of California, Los Angeles, 1982.

[33] J. Cawley, J. E. P. Metcalf, A. H. Jones, T. J. Band, D. S. Skupien, A Tribological Study of Cobalt Chromium Molybdenum Alloys Used in Metal-on-Metal Resurfacing Hip Arthroplasty, Wear, 255, 999-1006, (2003).

[34] L. Z. Zhuang, E. W. Langer, Effects of Cooling Rate Control during the Solidification Process on the Microstructure and Mechanical Properties of Cast Co-Cr-Mo Alloy Used for Surgical Implants, Journal of Materials Science, 24, 381-388, (1989).

[35] H. S. Dobbs, J. L. M. Robertson, Heat Treatment of Cast Co-Cr-Mo for Orthopaedic Implant Use, Journal of Material Science, 18, 391-401, (1983).

[36] L. Z. Zhuang, E. W. Langer, Effects of Alloy Additions on the Microstructures and Tensile Properties of Cast Co-Cr-Mo Alloy Used for Surgical Implants, Journal of Materials Science, 24, 4324-4330, (1989).

[37] J. Li, and W. Beres, Scratch test for coating/substrate systems–A literature review. Canadian Metallurgical Quarterly, 46(2), 155-173 (2007).

[38] R. Ahmed, Y. Q. Fu, N. H. Faisal, Fatigue at nanoscale: an integrated stiffness and depth sensing approach to investigate the mechanisms of failure in DLC film, ASME Journal of Tribology, Vol. 134(1), pp. 012001-012009, http://dx.doi.org/10.1115/1.4005774 (2012).

[39] H. H. Kim, S. H. Cho, C. G. Kang, Evaluation of microstructure and mechanical properties by using nano/micro-indentation and nanoscratch during aging treatment of rheo-forged Al 6061 alloy, Material Science and Engineering A, 485, pp. 272-281, (2008).

[40] A. M. Hodge, T. G. Nieh, Evaluating abrasive wear of amorphous alloys using nanoscratch technique, Intermetallics, 12, pp. 741-748, (2004).

[41] Y. Huang, L. Chiu, J. Shen, Y. Sun, J. J. Chen, Mechanical performance of metallic glasses during nanoscratch tests, Intermetallics, 18, pp. 1056-1061, (2010).

[42] R. Ahmed, A. Ashraf, M. Elameen, N. H. Faisal, A. M. El-Sherik, Y. O. Elakwah, M. F. A. Goosen, "Single Asperity Nanoscratch Behavior of HIPed and Cast Stellite 6 Alloys", Wear, In print (2014).

[43] D. Klarstrom, P. Crook, J. Wu, 2004, "Metallography and Microstructures of Cobalt and Cobalt Alloys", ASM Handbook, ASM Handbook, Volume 9: Metallography and Microstructures, G.F. Vander Voort, editor, p762–774, DOI: 10.1361/asmhba0003771.

[44] M. Yamaguchi, Y. Umakoshi, The operative slip systems and slip line morphology in βCuZn and β(CuNi)Zn alloys, Acta Metallurgica, 24(11), 1061-1067, (1976).

[45] M. Woldman, E. Van Der Heide, T. Tinga, M.A. Masen, The influence of abrasive body dimensions on single asperity wear, Wear, 301 76–81, (2013). http://dx.doi.org/10.1016/j.wear.2012.12.009

[46] K. Hokkirigawa, K. Kato, An experimental and theoretical investigation of ploughing, cutting and wedge formation during abrasive wear, Tribology International, 21(1), 51–57, (1988). http://dx.doi.org/10.1016/0301-679X

[47] A. Khellouki, J. Rech, H. Zahouani, Micro-scale investigation on belt finishing cutting mechanisms by scratch tests, Wear 308, 17–28, (2013). http://dx.doi.org/10.1016/j.wear.2013.09.016

[48] N. P. Suh, An Overview of the Delamination Theory of Wear, Wear, 44, 1-16, (1977).

Tables

Table 1. The chemical compositions of Stellite 21 alloy (wt.%)

Stellite	Co	Cr	Mo	C	Fe	Ni	Si	Mn
Stellite 21 (Cast)	Balance	28.48	6.03	0.26	0.51	0.24	0.65	0.48
Stellite 21 (HIPed)	Balance	27.80	5.5	0.28	1.55	2.74	1.66	0.82

Table 2. The sieve analysis of the Stellite powders (wt.%)

Stellite powder	+38µm	+20µm	-20µm
Stellite 21	0.00	50.5	49.5

Table 3. The area fraction of the individual phases in the Cast and HIPed alloys

Stellite alloy	Co-rich matrix	Cr-rich carbide	Mo-rich carbide
Stellite 21 (Cast)	Grey, 95 ± 0.7%	-	Light, 5.0 ± 0.7%
Stellite 21 (HIPed)	Grey, 93.3 ± 1.6%	Dark grey, 5.1 ± 0.8%	Light, 1.7 ± 0.8%

Table 4. The average hardness and Charpy impact energy results of cast and HIPed Stellite alloys (% change calculations exclude the differences in standard deviations; ISE (indentation size effect))

	Stellite 21 (Cast)	Stellite 21 (HIPed)	*change for HIPed*
Average Macro-hardness ($HV_{294\ N}$)	311.8 ± 6.3	351.2 ± 2.3	*+12.6%*
Average Micro-hardness ($HV_{2.94\ N}$)	370.1 ± 26.2	371.8 ± 16.3	-
% change between average macro- and micro-hardness (ISE)	*+18.7%*	*+5.8%*	-
Average Nanohardness (50mN load) - GPa	7.8 ± 1.9	9.3 ± 0.6	*+19.7*
Maximum hardness relating to carbide (50mN load) - GPa	11.2 ˜ 14.4	10.1 ˜ 10.3	
Minimum hardness relating to metal matrix (50mN load) - GPa	5.9 ˜ 6.9	7.9 ˜ 8.8	
Average Nanohardness (5mN load) - GPa	11.2 ± 4.6	10.3 ± 4.2	*-7.9%*
Maximum hardness relating to carbide (5mN load) - GPa	17 ˜ 22	17.2 ˜ 17.4	
Minimum hardness relating to metal matrix (5mN load) - GPa	8.5 ˜ 8.9	8.5 ˜ 9.3	
% change between average nanohardness at 50mN and 5mN load (ISE)	*+43.8*	*+10.7*	
Unnoteched Charpy impact energy (J)	125.3± 33.8	94.5± 5.1	

Table 5. Tensile test results for HIPed alloy

Alloy	Elastic Modulus (GPa)	Yield strength (0.2%) (MPa)	Ultimate Tensile Strength (MPa)	Elongation (%)
Typical expected values (HIPed alloy) *	245	650	1000	~20
Typical expected values (cast alloy) *	250	565	710	9
Stellite 21 HIPed alloy, as measured	244.6±5.4	510.4±5.2	941.1±23.9	6.1±1.7

***** Deloro Stellite; Stellite 21 Technical Data Sheet, 2008, DS01-22208 (S R0808) [23]

Table 6. The chemical compositions of cast HIPed Stellite 21 alloys (atomic %).

Alloy	Co	Cr	Mo	C	Si	Fe+Ni	Total others incl. Mn	Ratio [Cr+Mo]/C	Ratio [Cr]/C	Ratio [Mo]/C	Observed carbides
Cast	61.3	31.2	3.6	1.2	1.3	0.7	<1.0	28.21	25.30	2.9	$M_{23}C_6$
HIPed	57.0	30.1	3.2	1.3	3.3	4.2	<1.0	25.39	22.93	2.46	$M_{23}C_6$ M_6C (SEM only)

Figures

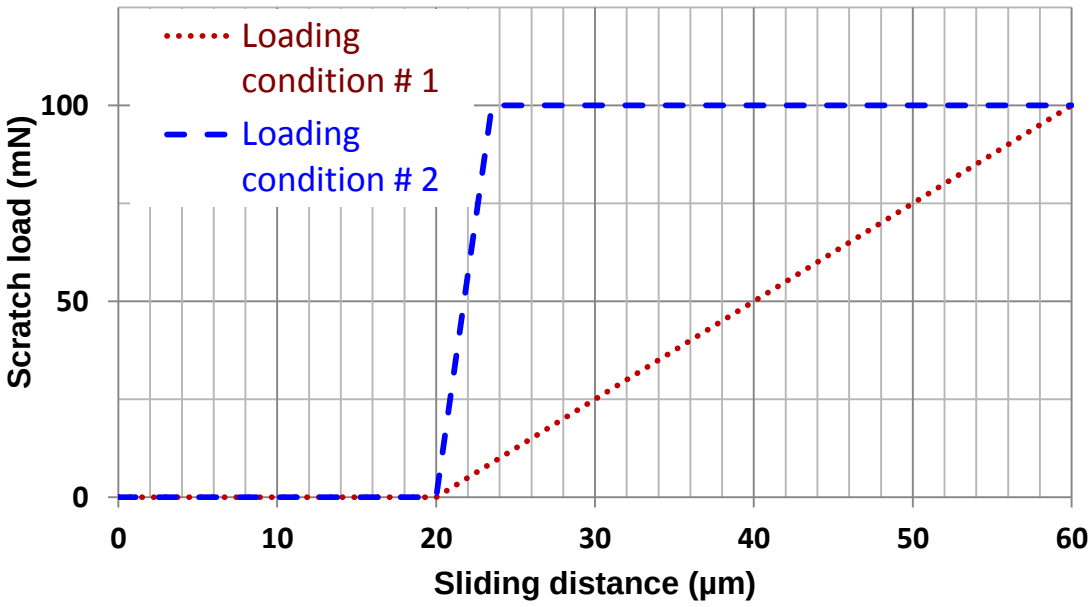

Figure 1. Loading conditions used for scratch testing. Load was ramped linearly after 20 μm travel at 5 mN/s to reach 100 mN for loading condition 1 (2 μJ). For the loading condition 2 (3.83 μJ), the load was increased linearly after 20 μm travel at 50 mN/s to reach 100 mN.

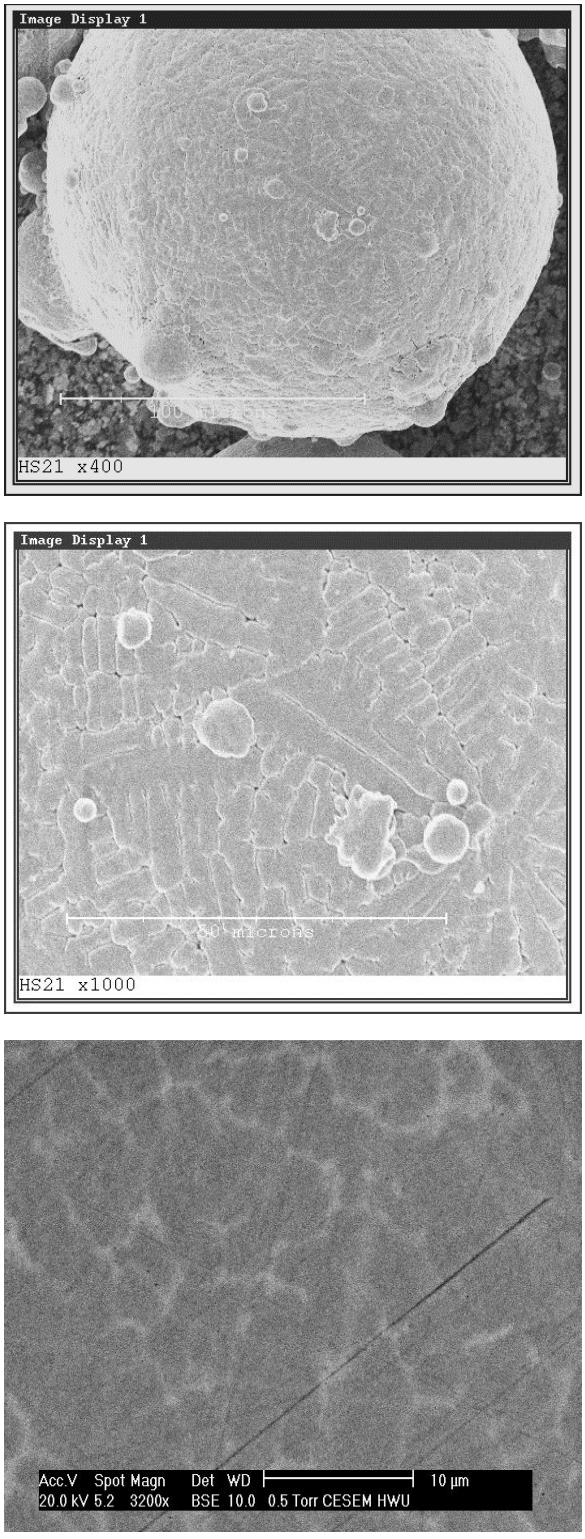

Figure 2. Stellite 21 morphology: (a) SEM (SE) image showing the powder particle, (b) surface morphology of powder particle, and (c) SEM (BSE) image showing the powder particle cross-section. Scale marker in (a) is 100 µm, in (b) is 50 µm and in (c) is 10 µm.

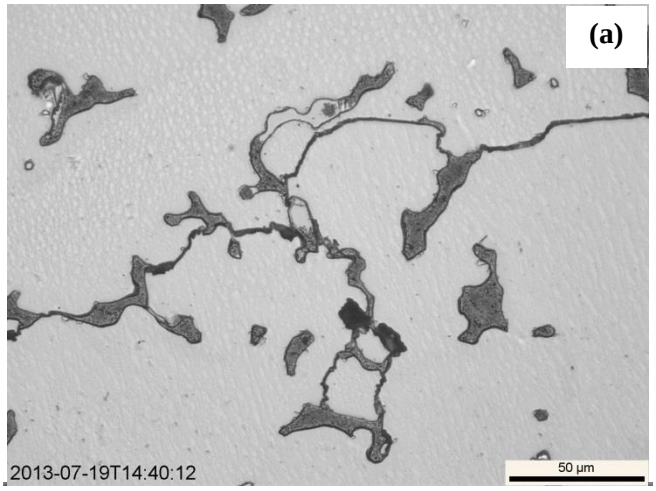
(a)
2013-07-19T14:40:12
50 µm

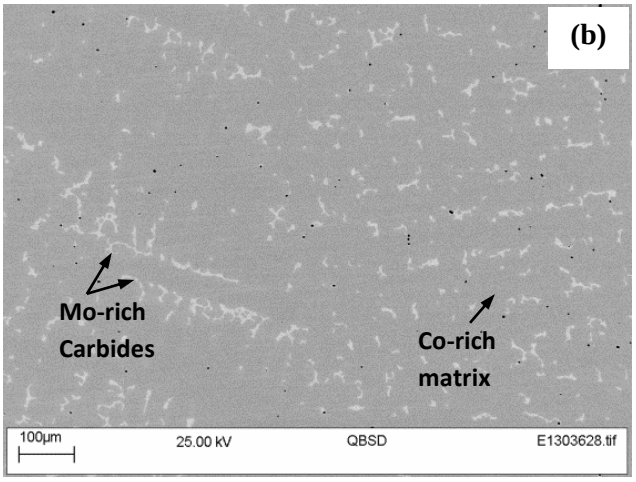
(b)
Mo-rich
Carbides
Co-rich
matrix
100µm
25.00 kV
QBSD
E1303628.tif

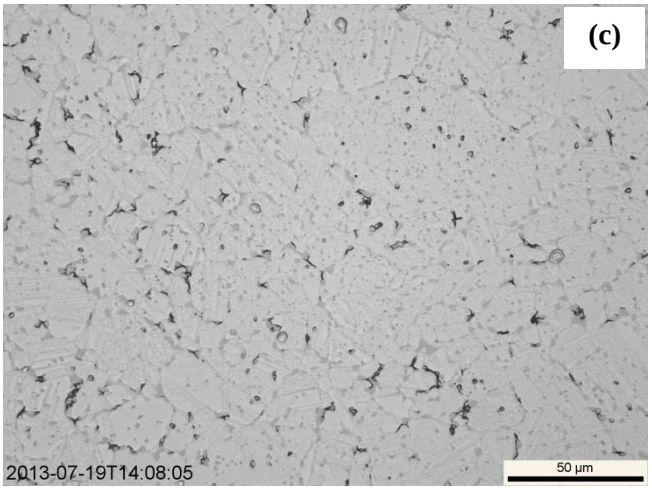

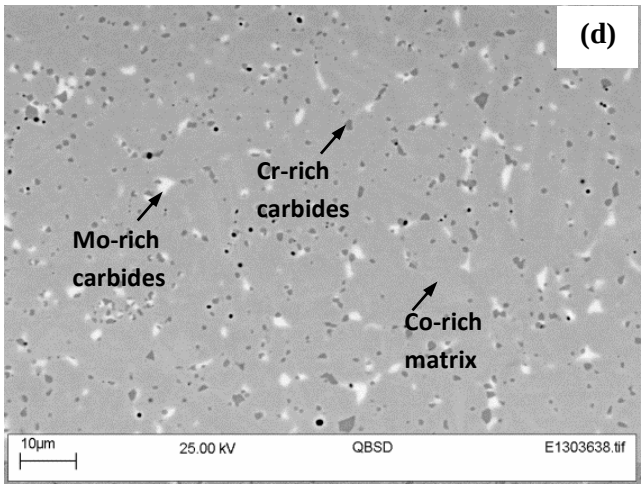

Figure 3. The microstructure of Stellite 21: (a) cast Stellite alloy (etched optical image); (b) cast Stellite alloy (SEM (BSE) image); (c) HIPed Stellite alloy (etched optical image); (d) HIPed Stellite alloy (SEM (BSE) image). (Etching was done by immersing in a solution of 5 ml HNO_3, 200 ml HCl, 65g $FeCl_3$ for few seconds).

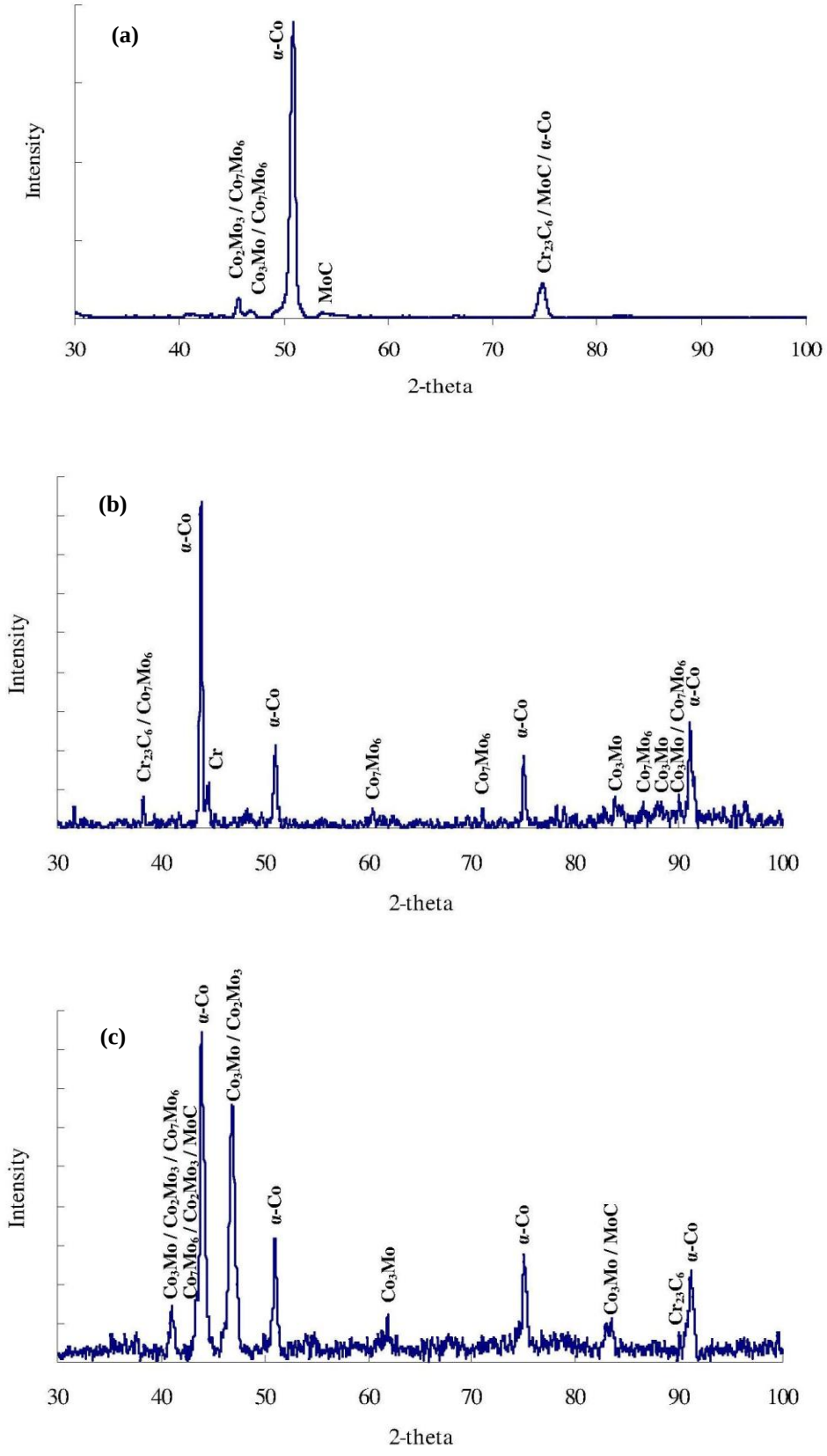

Figure 4. XRD diffractogram of the Stellite 21: (a) cast Stellite alloys, (b) powder, and (c) HIPed Stellite alloys.

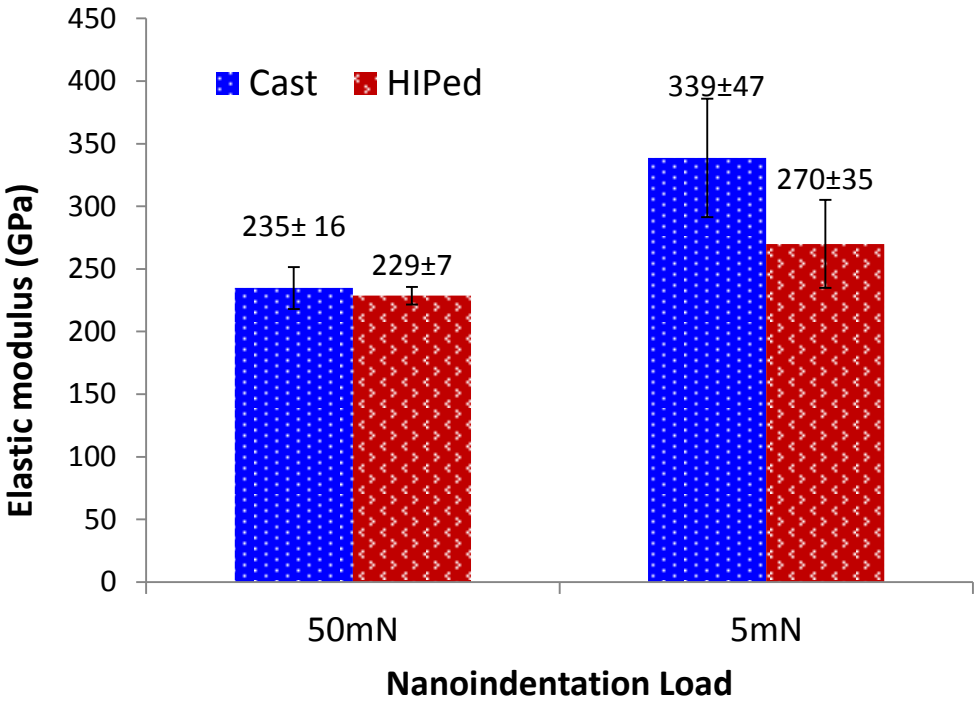

Figure 5. Nanoindentation elastic modulus results of cast and HIPed Stellite 21 alloys (average values and standard deviation labelled on the columns).

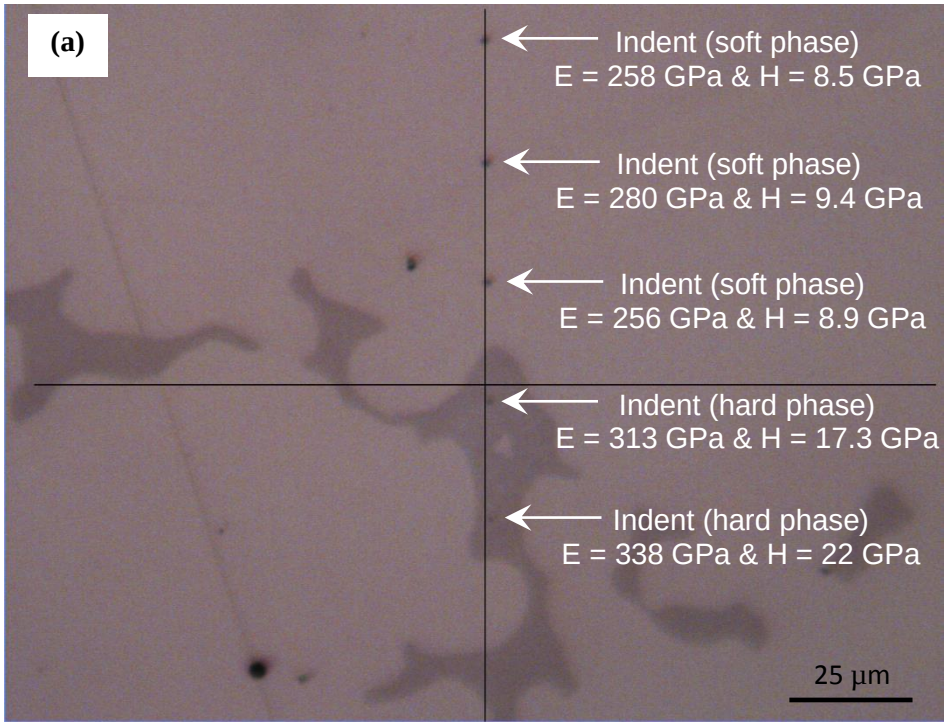
(a)
Indent (soft phase)
E = 258 GPa & H = 8.5 GPa
Indent (soft phase)
E = 280 GPa & H = 9.4 GPa
Indent (soft phase)
E = 256 GPa & H = 8.9 GPa
Indent (hard phase)
E = 313 GPa & H = 17.3 GPa
Indent (hard phase)
E = 338 GPa & H = 22 GPa
25 µm

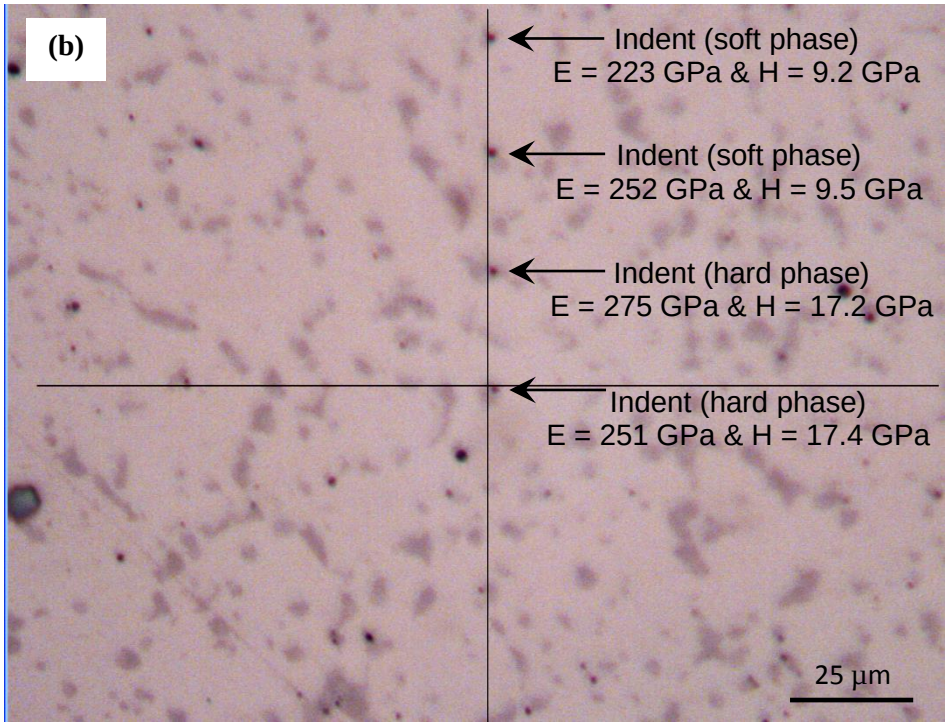

Figure 6. Location of nanoindentations at 5mN load on (a) cast Stellite 21 and (b) HIPed Stellite 21 alloys (E is the Elastic modulus and H is hardness of individual indents).

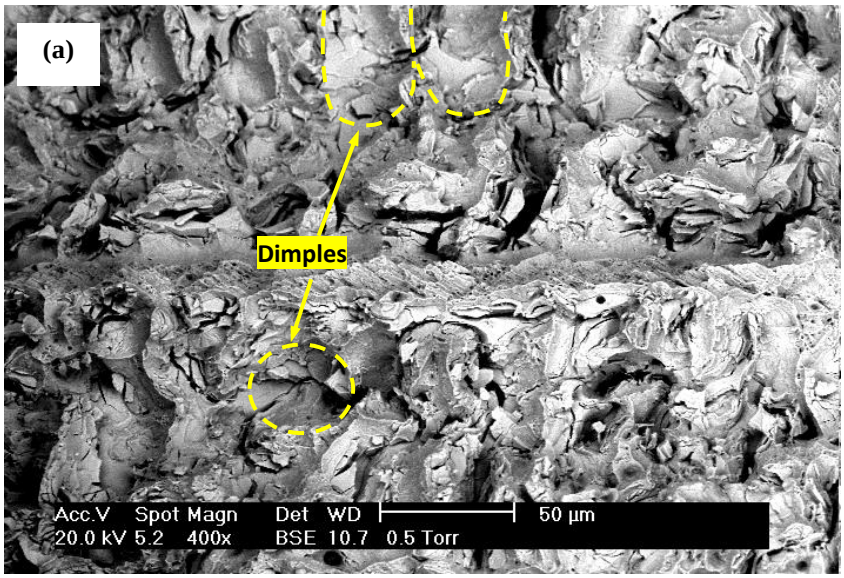

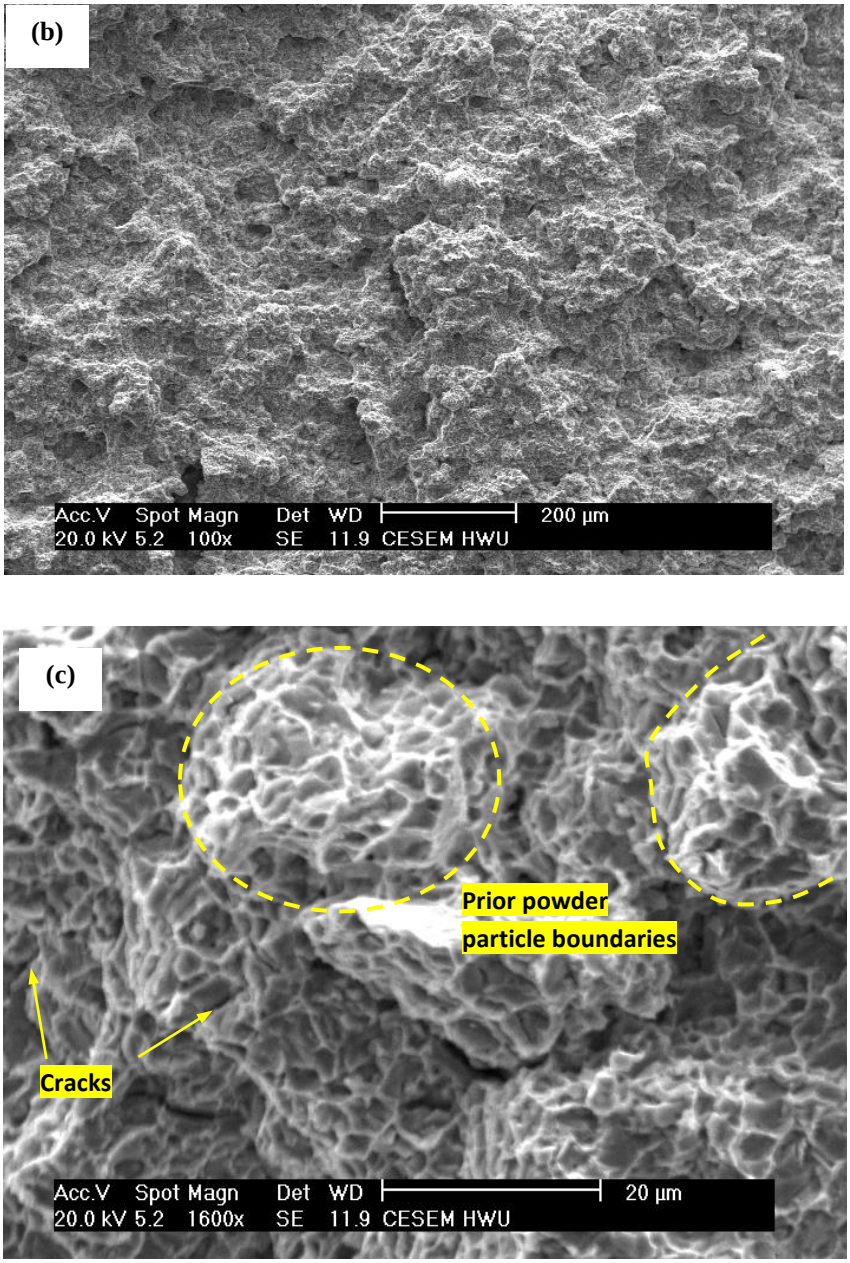

Figure 7. The SEM fractographs after the Charpy impact test on, (a) cast Stellite alloy (BSE), (b) HIPed Stellite alloy (SE), (c) HIPed alloy at higher magnification (SE).

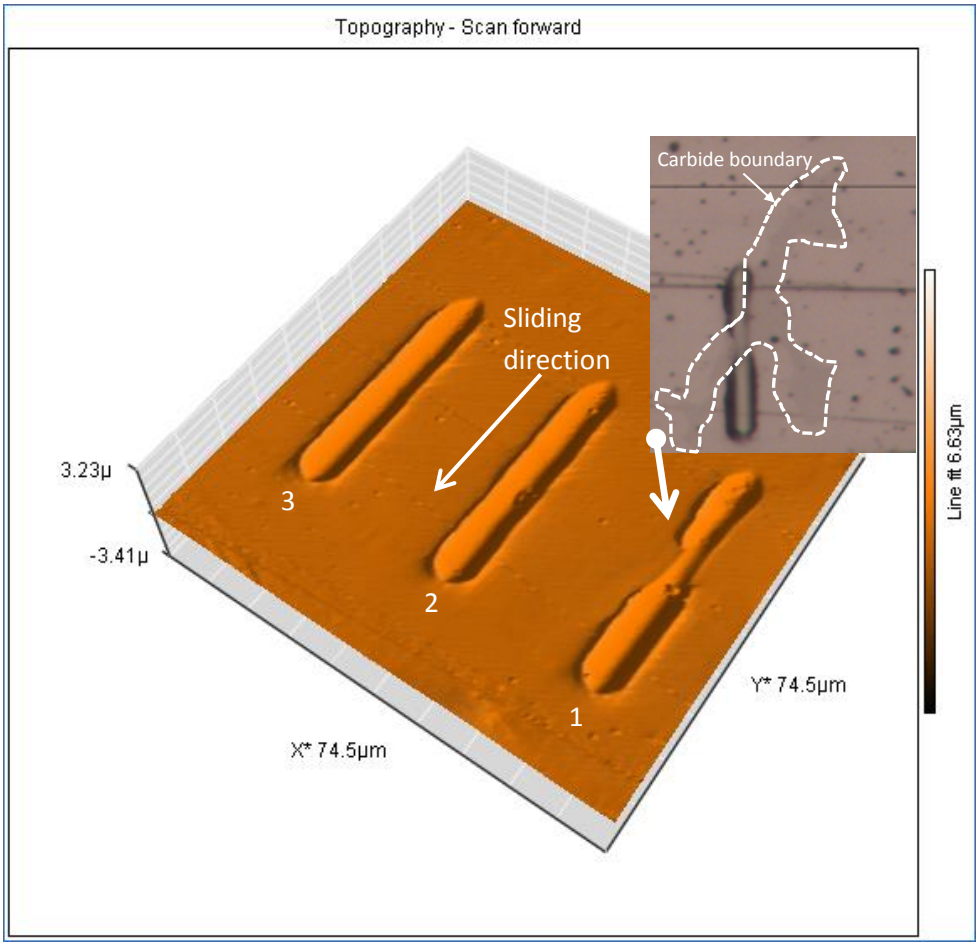
Topography - Scan forward
Carbide boundary
Sliding
direction
3.23µ
-3.41µ
3
2
1
Y* 74.5µm
X* 74.5µm
Line fit 6.63µm

a)

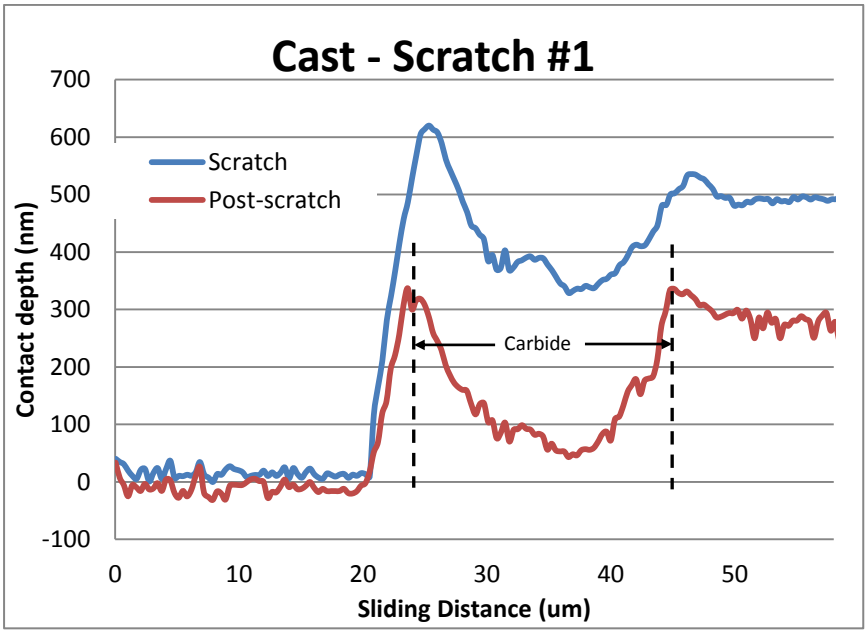
Cast - Scratch #1
Scratch
Post-scratch
Carbide
Contact depth (nm)
Sliding Distance (um)
700
600
500
400
300
200
100
0
-100
0
10
20
30
40
50

b)

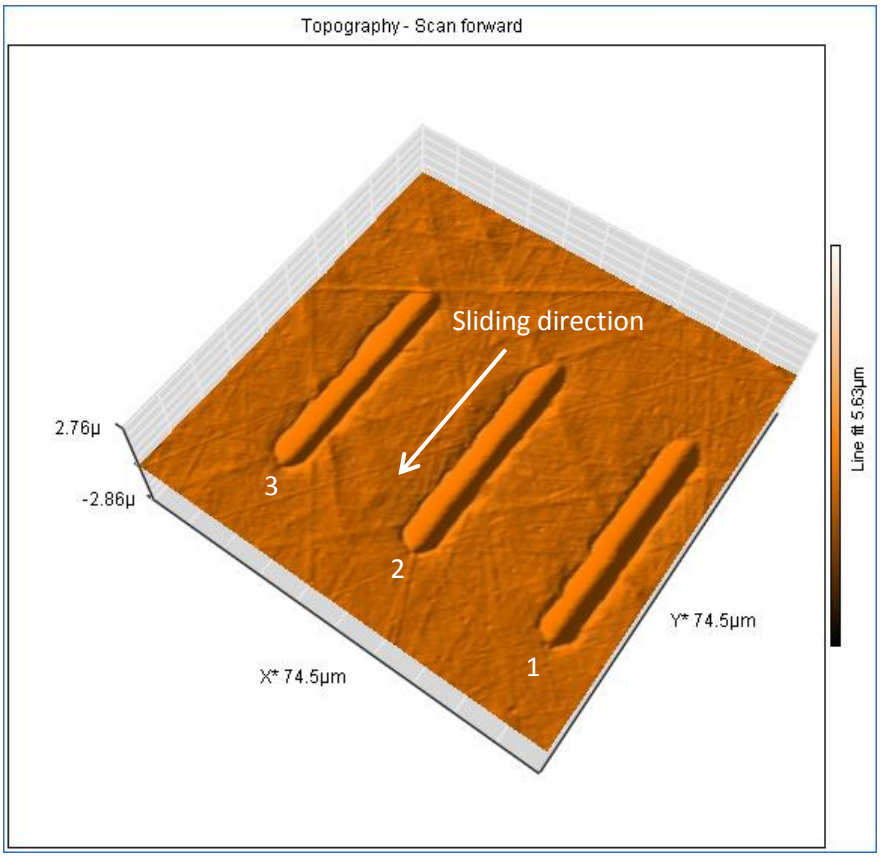

c)

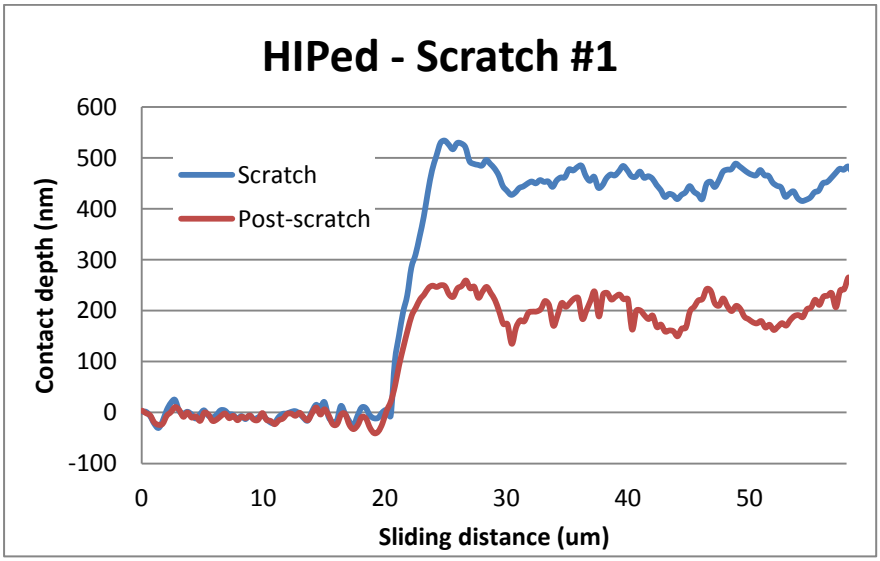

d)

Figure 8. Comparison of scratch morphology between cast and HIPed Stellite 21 alloys for loading condition 2; (a) AFM topography map of scratches 1, 2 and 3 for cast alloy; (b) pre and post-scan depth profile of wear scar 1 for cast alloys; (c) AFM

topography map of scratches 1, 2 and 3 for HIPed alloy; (d) pre and post-scan depth profile of wear scar 1 for HIPed alloy.

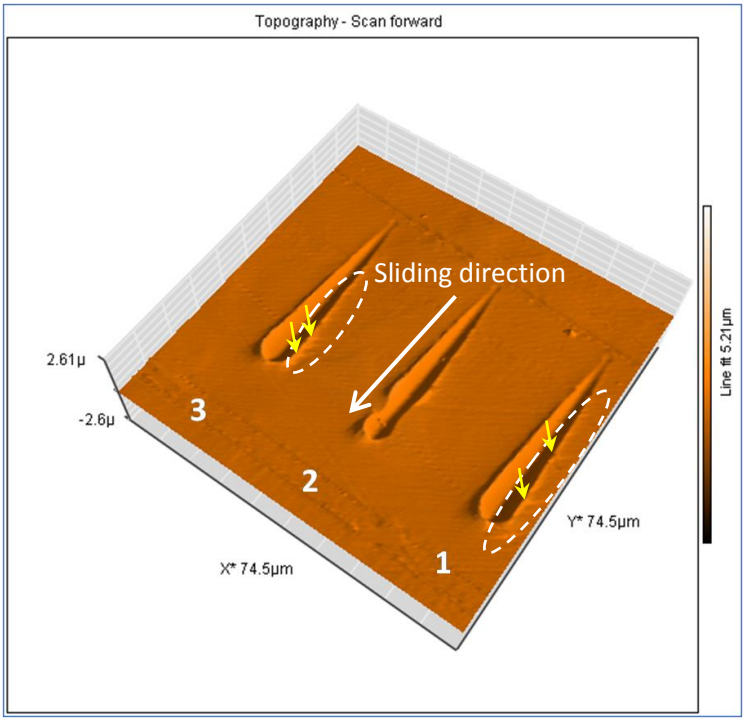

a

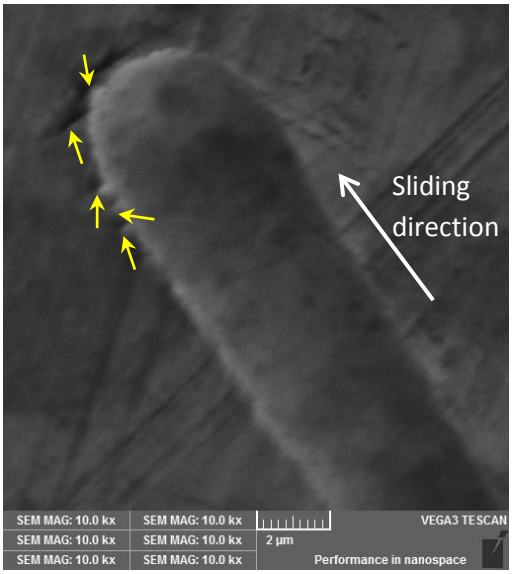

b)

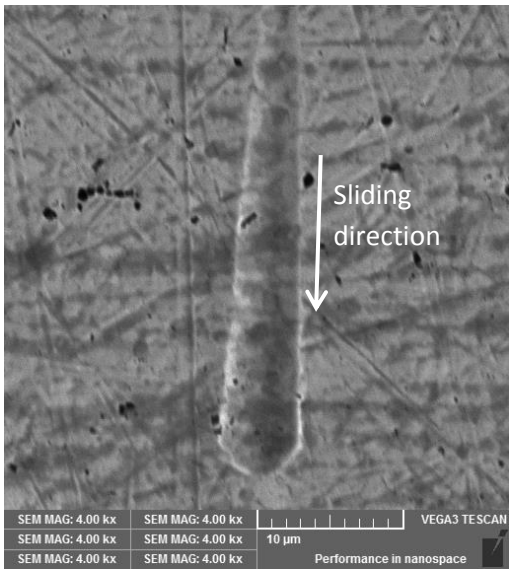

c)

Figure 9. Surface observations of wear scars for loading condition # 1; (a) AFM topography map scratches 1, 2 and 3 of cast Stellite 21 alloy; (b) SEM (SE) observation of the end of wear scar for cast alloy; (c) SEM (SE) observation of scratch for HIPed alloy.

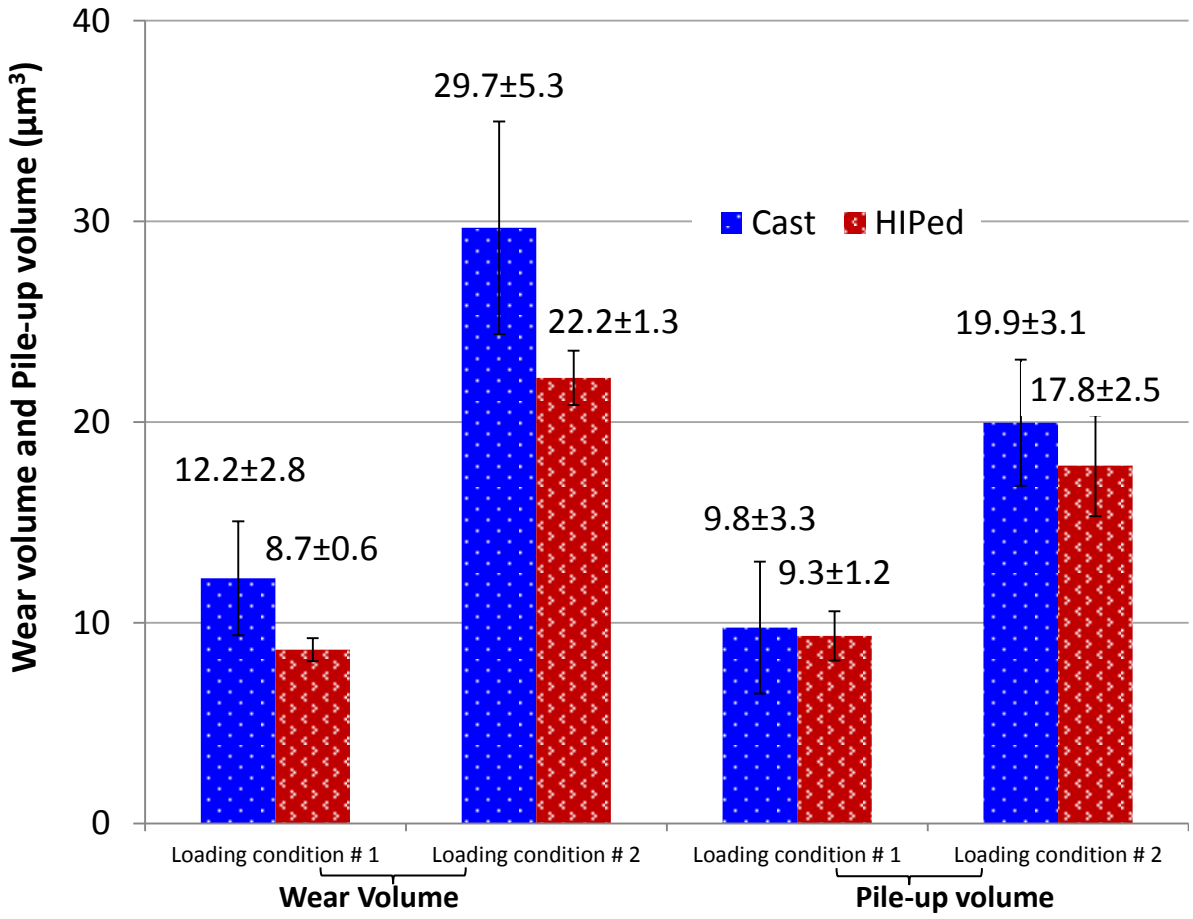

Figure 10. Average wear volume and pile-up volume for loading conditions 1 and 2 (average values and standard deviation labelled on the columns).

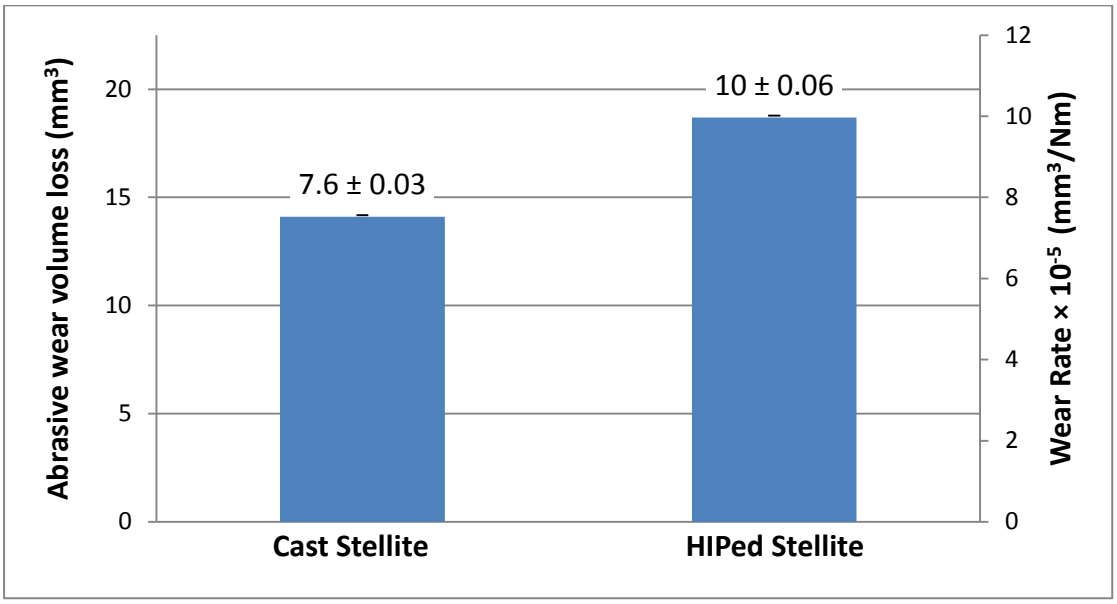

Figure 11. The wear volume loss after dry sand rubber wheel (DSRW) tests of cast Stellite 21 and HIPed Stellite 21 alloys (average values and standard deviation of wear rate also labelled on the columns).

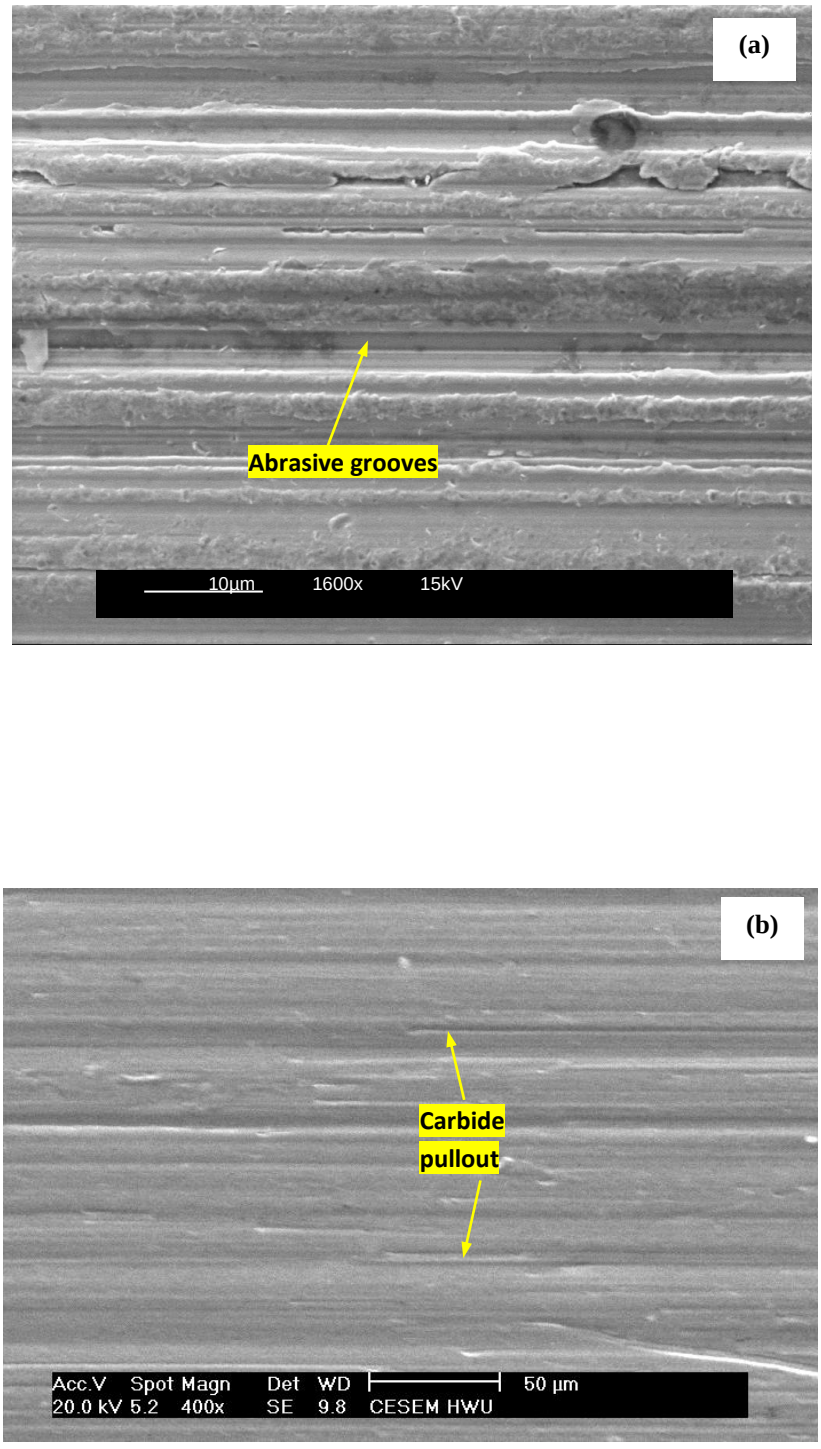

Figure 12. SEM (SE) observations of the wear scars after the abrasive wear (DSRW) tests on Stellite 21 alloys: (a) cast Stellite, and (b) HIPed Stellite.

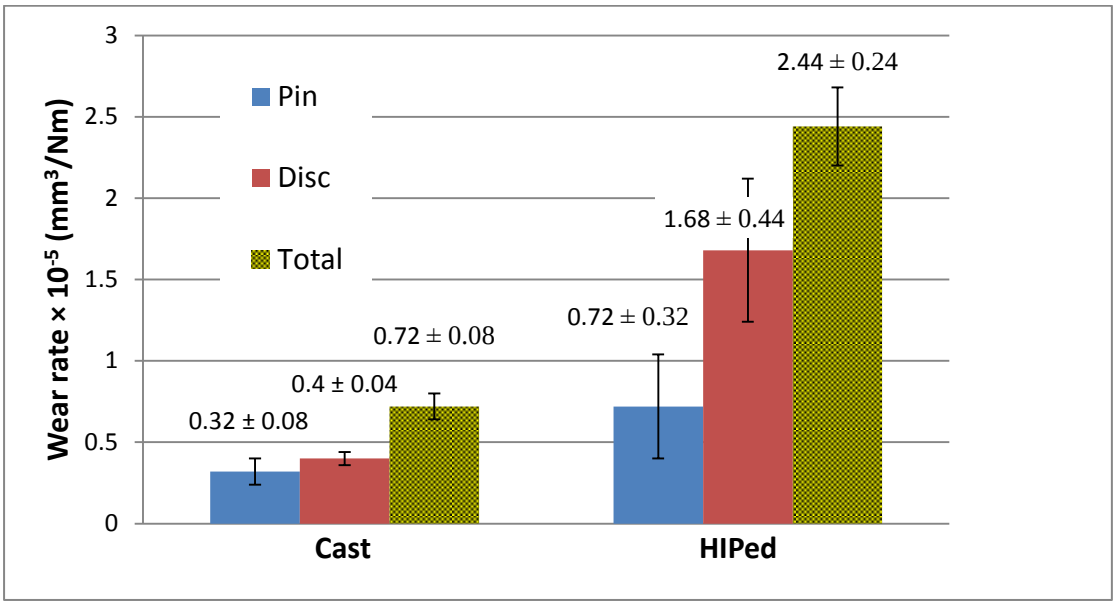

Figure 13. The self-mated pin-on-disc test results of cast and HIPed Stellite 21 alloys (average values and standard deviation labelled on the columns).

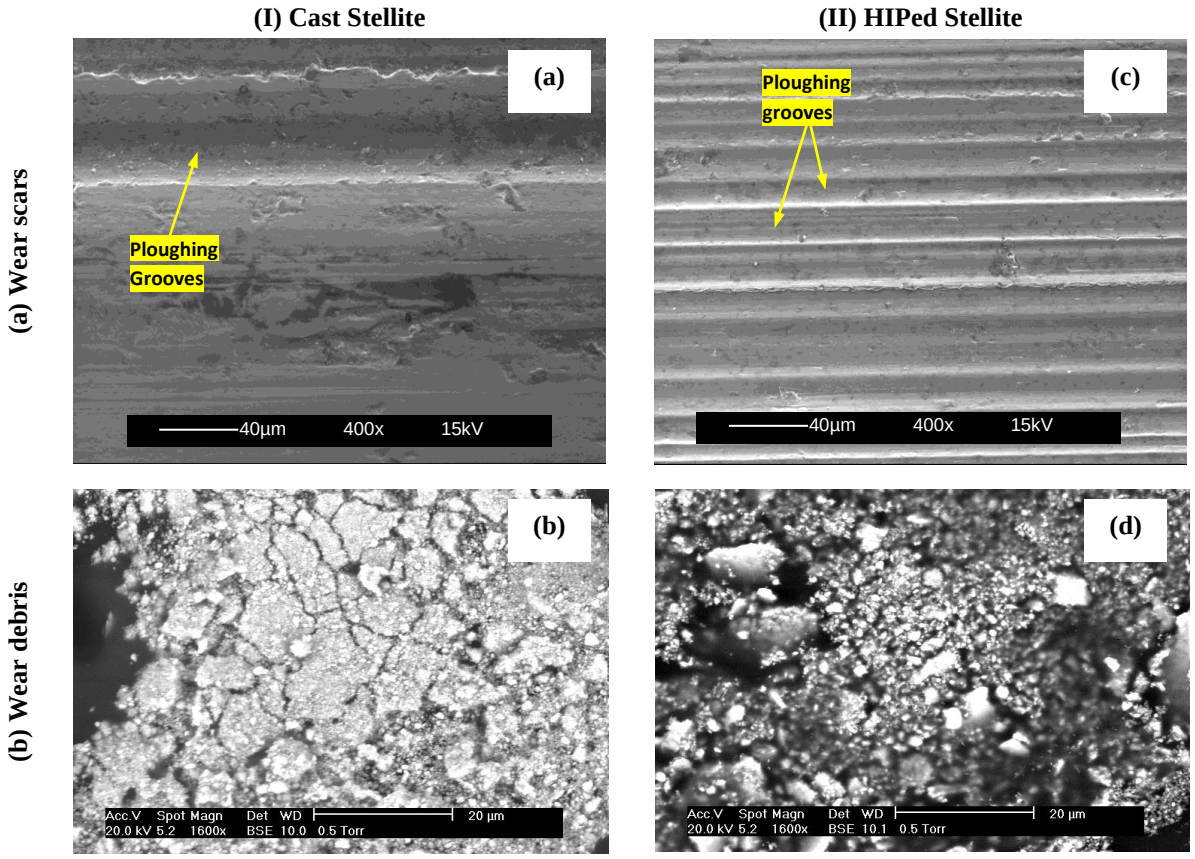

Figure 14. SEM observations of the wear scars and debris after the self-mated pin-on-disc tests on Stellite alloys 21: (I) cast Stellite (a (SE), b (BSE)), and (II) HIPed Stellite (c (SE), d (BSE).

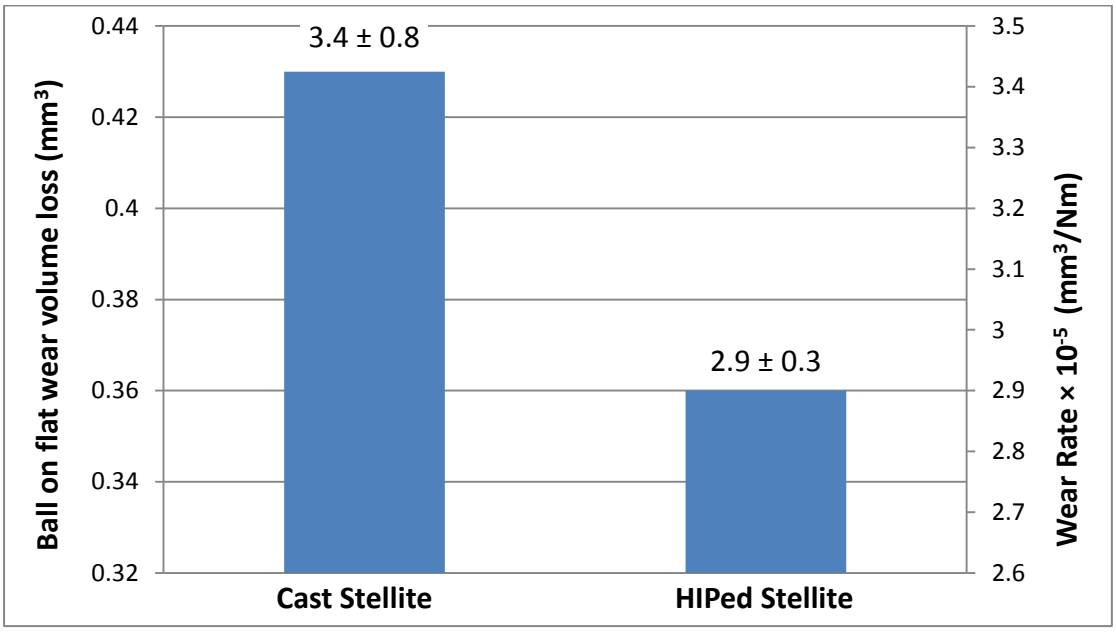

Figure 15. The ball-on-flat test results of cast and HIPed Stellite 21 alloys (average values and standard deviation of wear rate is labelled on the columns).

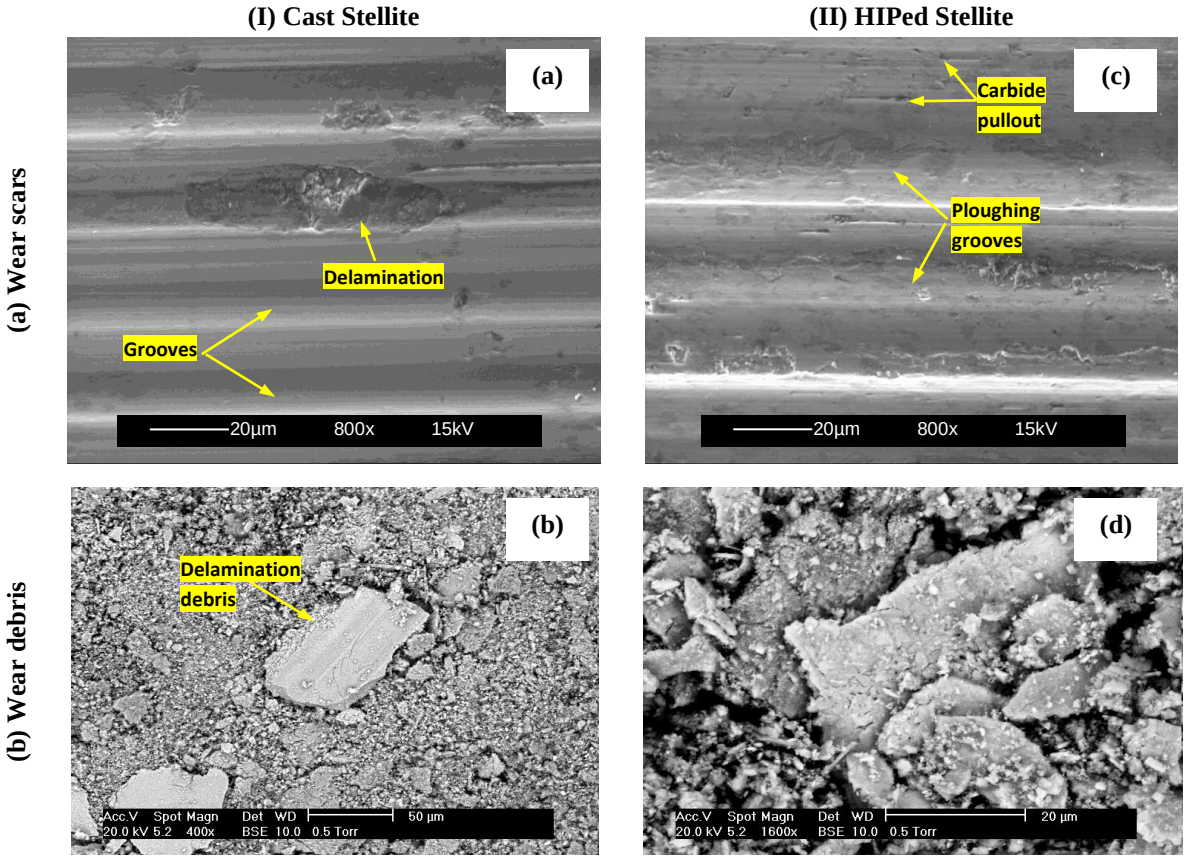

Figure 16. SEM observations of the wear scars and debris after the ball-on-flat test results on Stellite alloys 21: (I) cast Stellite (a (SE), b (BSE)), and (II) HIPed Stellite (c (SE), d (BSE)).

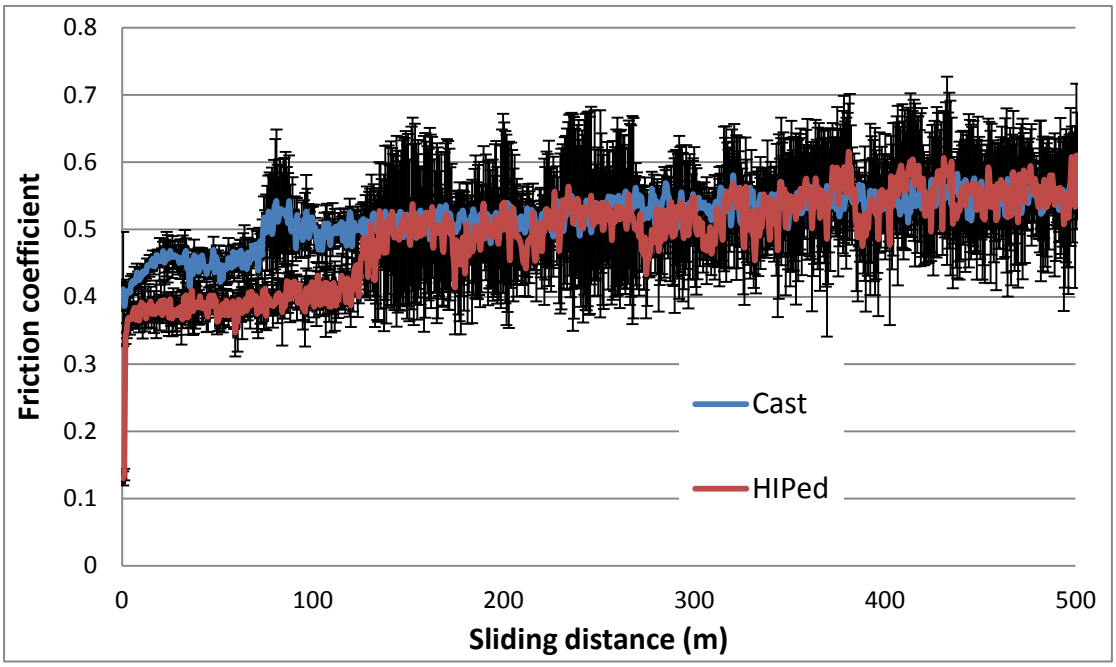

Figure 17. Averaged friction coefficient values for ball-on-flat tests (standard deviation of averaged data points is also indicated)

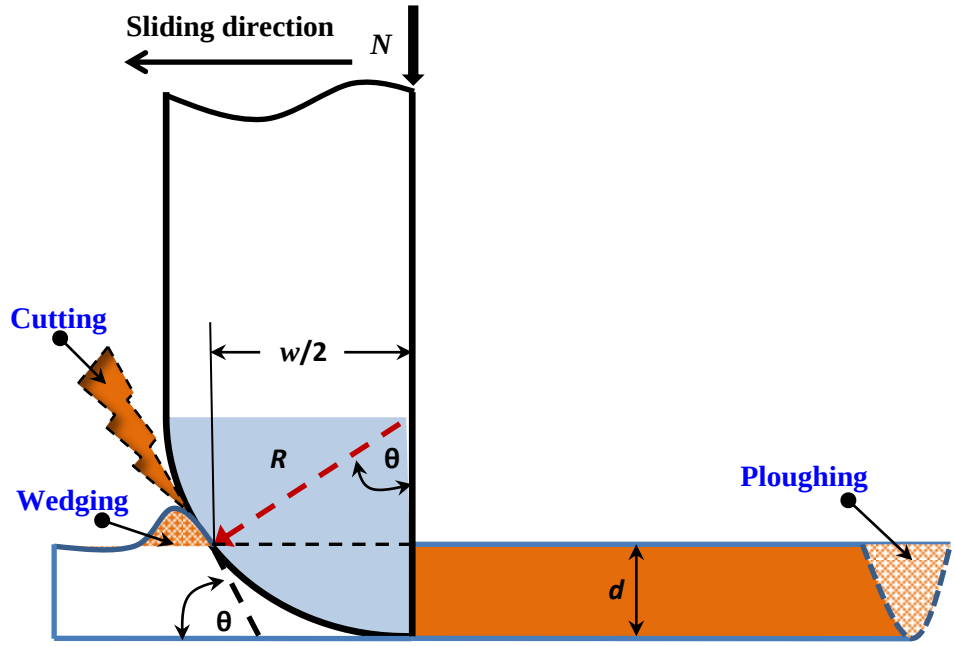

Figure 18. Schematic of ploughing, wedging and cutting in single asperity sliding contact